Three-dimensional elastic analysis of a bi-material system with a single domain boundary element method

Chunlin Wu[b], Liangliang Zhang[a,*], Junhe Cui[b], Huiming Yin[b,*]

[a]*Department of Applied Mechanics, China Agricultural University, 301 Yifu Building 17 Qinghua East Road, Beijing, 100083*

[b]*Department of Civil Engineering and Engineering Mechanics, Columbia University, 610 Seeley W. Mudd 500 West 120th Street, New York, 10027*

Abstract

The three dimensional fundamental solution of bi-materials is introduced to the boundary element method (BEM) for elastic analysis of a bi-material system instead of solving a multi-domain problem. Using the explicit form of the Green's function for bi-materials, the boundary integral equations (BIE) are set up for a finite bi-layered material system with a plane interface. The Green's function for a bi-material system combines the Kelvin's solution and disturbed fields by image source. Because it exactly satisfies the jointed continuity conditions at the interface ($x_3 = 0$), no internal mesh is required along the interface and a single domain BEM can be established. The potential numerical errors of the multi-domain BEM using the Kelvin's solution due to the mesh quality at the interface can be avoided. This single domain BEM for bi-material saves the effort of domain discretization, predicts the singularity on the interface analytically, and enables an efficient, straightforward analysis similar to the homogeneous solids. It is particularly suitable to simulate thin film/substrate systems, overlay/base structures, and other similar layered materials. The numerical simulations verify the effectiveness and convergence of the method, and the case studies of wind turbine blades and solar panels demonstrate the industrial applications of this method.

Keywords: Boundary element method, Green's function, Bi-layered material systems, Interfacial stress, Elastic analysis

1. Introduction

For an infinite domain containing two jointed dissimilar half-spaces of homogeneous isotropic materials, the elastic field caused by a point force can be determined by the Green's function. In

*Corresponding author. Tel.: +1 212 851 1648, +86 010 62736411; Fax: +1 212 854 6267

Email addresses: cw3056@columbia.edu (Chunlin Wu), llzhang@cau.edu.cn (Liangliang Zhang), jc5614@columbia.edu (Junhe Cui), yin@civil.columbia.edu (Huiming Yin)

literature, Michell [1], Love [2] among others [3] have derived the elastic solution in two jointed half-spaces with different interface conditions, such as complete weld or direct stresses transmission and their approach is to utilize the corresponding harmonic potentials. Mindlin [4] proposed the fundamental solution of elastic field of a semi-infinite domain under a concentrated force, namely the Mindlin's solution, which was further derived to a concise form of the Galerkin vector stress functions [5]. Rongved [6, 7] extended the solution to the semi-infinite domain with fixed boundary condition. Kuo and Mura [8] and others [9, 10] investigated problems of dislocation or disinclination loops. For pure dilation (caused by the nuclei of strain), Mindlin and Cheng [11] and Sen [12] considered the thermal-elastic stresses, which were known as hydrostatic inclusions.

The solution has been extended to bi-materials by Yu and Sanday [13], Yu et al. [14], Tinti and Armigliato [15] and Singh et al. [16]. By generalizing Collin's work [17], Walpole [18] proposed an explicit solution of two jointed isotropic half-spaces through the method of images, which can be reduced to Lorentz's, Mindlin's and Stokes flow problems [19, 20] by adjusting the material properties [21]. In addition to the investigation of isotropic materials, pioneers devoted efforts to derive closed-form solutions to transversely isotropic media with horizontal or inclined planes of isotropy [22], which is generally applied to geomechanics. Divided by the various loading types, Pan and Chou [23] and others [24–28] solved cases of concentrated point loads; Wang and Liao [29] and others [30–33] considered load distribution patterns of ring, rectangle, etc. Furthermore, Yue formulated the fundamental singular solution to multi-layered media [34–36] in an integral form, which has been named as Yue's treatment.

Although the closed-form fundamental solutions have been investigated for various types of problems, such as a half-space with different boundary conditions on the surface and two fully bonded semi-spaces, those solutions are often obtained under the assumption of an unbounded space. For finite domain problems, however, numerical methods, such as finite element method (FEM), BEM and their extensions, have been commonly used. As a domain discretzation method, the simulation of bi-material with FEM generally requires assigning different material properties to elements in two material phases, and a large number of elements are needed due to the singularity and discontinuity caused by the material mismatch. Several studies focused on the stress intensity factors (SIFs) at crack-tip or interfacial inhomogeneities. Among them, Oyadiji's group [37, 38] proposed the fractal-like FEM (FFEM) to analyze the SIFs of V-notch and notch bodies, which employs the displacement fields as global interpolation functions. Pathak et al. [39] and Bouhala et al. [40] used extended FEM (XFEM) for crack-tip at the interface of bi-material. Kaddouri et

al. [41] investigated several factors related to the crack deflection, such as elastic moduli of two materials, thickness of the bi-material, etc.

BEM can be a good alternative to FEM as it can calculate local fields by boundary integrals. However, for a bi-material system, the multi-region BEM has been commonly used [42, 43] with Kelvin's solution, and the interface of two material phases shall be discretized with a refined mesh due to the effect of singularity. In literature, Cheng et al. [44] and Gu and Zhao [45] extends the multi-region BEM to investigate stress singularities at V-notch and crack-tips, respectively. Several researchers proposed to use the infinite element techniques to simulate far-field effects of the half-space [43, 46, 47]. Ai et al. [48, 49] analyzed the piles in multi-layered soils with ALEM. Such discretization technique, however, will surely influence the accuracy and efficiency of the solutions, because more elements and equations are involved in the system. To address the above issue, the authors [22, 50] utilizes Yue's treatment to simulate bi-material with inclined planes of isotropy and multi-layer half-space problems, respectively. Yue's treatment enables numerical simulation by a single-region, which saves efforts of interface mesh [35, 36] and is applicable to multi-layered solids, and it can also be simplified for bi-material (two-layered material) as well. However, compared with Walpole's solution [18], it does not have an explicit form and is complicated to be implemented.

Yuuki et al. [51] applied the Hentenyi's fundamental solution and developed a single domain BEM for two-dimensional (2D) bi-material problems with vertical straight interface. Subsequently, Lou and Zhang [52] extended the algorithm for two-dimensional elastoplastic bi-material problems and investigated stress fields of elliptic hole under simple tension. However, their work were limited to 2D problems, which could be caused by the unavailability of the explicit form of the Green's function for 3D bi-materials at the time. With the recent work from Walpole [18] and our group [20], this paper extends the work to 3D for wide applications among the research and engineering community.

This paper aims to perform elastic analysis of a bi-material system composed of two jointed dissimilar isotropic phases with a single domain BEM implemented with Walpole's fundamental solution [18]. In Section 2, the bi-material problem is described with certain boundary conditions. Without the loss of any generality, the interface plane S is selected at $x_3 = 0$; for cases with inclined interface plane, the elastic stress analysis can be completed by coordinate transformation while keeping the Green's function same. In Section 3, the BEM with Walpole's solution is formulated. Because Walpole only considered the case when source points exist in the upper phase $x_3' \geq 0$, the solution can be completed through method of images [18, 21] by switching the field and source

points. Alternatively, the method of symmetry is applied and the derivatives of Green's function are provided in Appendix A. Subsequently, numerical results of panels with tractions are compared with FEM outputs to validate the BEM model in Section 4. In Section 5, the model is employed to analyze some popular industrial applications, such as wind turbine blades and solar panels. In Section 6, a parametric study is conducted on effects of thickness ratio and shear modulus of the two phases.

2. Problem Statement

Consider domain $\mathcal{D}$ composed of two material phases, where the upper phase $\mathcal{D}^+$ and the lower phase $\mathcal{D}^-$ exhibit homogeneous isotropic elastic behaviors as $\mathcal{C}'$ and $\mathcal{C}''$, respectively, in Fig. 1. In the following, μ and ν stand for shear moduli and Poisson's ratio, respectively, and $\mathcal{C}'_{ijkl} = \frac{2\mu'\nu'}{1-2\nu'}\delta_{ij}\delta_{kl} + \mu'(\delta_{ik}\delta_{jl} + \delta_{il}\delta_{jk})$, and similarly to $\mathcal{C}''$. The domain $\mathcal{D}$ is subjected to prescribed boundary conditions shown in Fig. 1, where $\mathbf{t}$ and $\mathbf{u}$ represent stress and displacement loads applied on the boundary, respectively. Without the loss of any generality, the interface surface S is set parallel to $x_1 - x_2$ plane with $x_3 \equiv 0$; for cases with inclined or shifted interface S, coordinate transformation can be utilized without changing the Green's function. Following Walpole's work [18], the interface S is assumed to be perfectly connected without any possibility of debonding so that the continuity equations must be satisfied as follows:

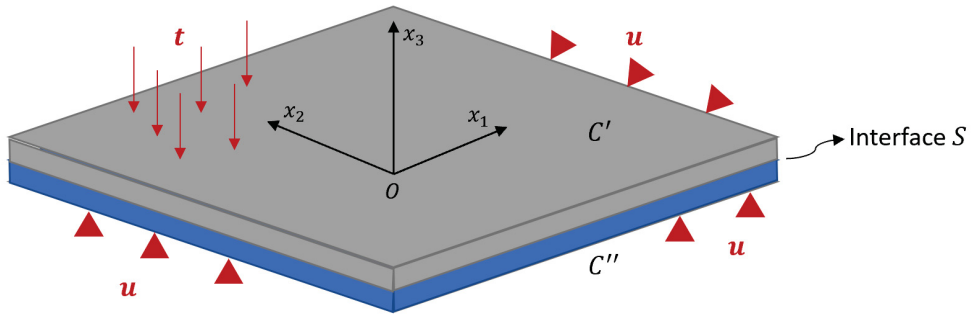

Figure 1: Schematic illustration of domain $\mathcal{D}$ composed of two dissimilar isotropic material phases with prescribed boundary conditions and the continuous interface

$$\begin{aligned} u_i^+(\mathbf{x}) &= u_i^-(\mathbf{x}) \quad \text{on } S \\ \sigma_{ij}^+(\mathbf{x})n_j^+ &= \sigma_{ij}^-(\mathbf{x})n_j^- \quad \text{on } S \end{aligned} \tag{1}$$

where superscripts "+" and "-" represent the upper and lower sides of the interface S; $\mathbf{n}^{\pm} = (0, 0, \mp 1)$ is the normal vector of interface S for the two cases. Hence, the boundary value problem is formulated on the prescribed boundary conditions and interfacial continuity equations, and can be solved with multi-region scheme [43] by discretizing both the interface S and the boundary, which typically requires a very fine mesh to obtain convergent solution due to the stress singularity along the interface. In most cases, the elastic stiffness tensors ($\mathcal{C}'$ and $\mathcal{C}''$) are finite and non-zero. However, the Green's function for half-spaces can be obtained through adjusting the stiffness tensors for the Green's function of a bi-material domain. For the bi-material system in Fig. 1, its Green's function takes into account of the interface effect analytically, so no mesh is needed. The boundary effects of a bi-material system can be evaluated by the boundary integral of a bi-material system, so that a single-domain BEM for a finite bi-material system can be developed and demonstrated.

3. Formulation of boundary element method

3.1. Fundamental solution for a bi-material infinite domain

Considering an infinite space composed of two dissimilar isotropic half-spaces, the fundamental solution to the displacement field can be derived through superposition of Kelvin's solution and image solution. Walpole [18] provided the explicit fundamental solution when the source point $\mathbf{x}'$ is located in the upper phase as Eq.(2) and Eq.(3) in terms of the positions of field point $\mathbf{x}$ as follows,

(1) When $x_3 > 0$ and $x_3' > 0$

$$\begin{aligned} 4\pi\mu' G_{ij}^{u}(\mathbf{x},\mathbf{x}') = {} & G_{ij}^{Ku}(\mathbf{x},\mathbf{x}') + A^{u}\overline{\phi}\delta_{ij} + B^{u}(\delta_{i3}\delta_{jk} - \delta_{ik}\delta_{j3})\overline{\alpha}_{,k}^{u} \\ & - C^{u}x_3\left[Q_J\overline{\psi}_{,ij3} + 4(1-\nu')\delta_{j3}\overline{\phi}_{,i} + 2(1-2\nu')\delta_{i3}Q_J\overline{\phi}_{,j} - Q_J x_3\overline{\phi}_{,ij}\right] \\ & - D^{u}Q_IQ_J\overline{\psi}_{,ji} - (G^{u}+B^{u})Q_J\overline{\beta}_{,ij}^{u} \end{aligned} \tag{2}$$

(2) When $x_3 < 0$ and $x_3' > 0$

$$\begin{aligned} 4\pi\mu' G_{ij}^{u}(\mathbf{x},\mathbf{x}') = {} & G_{ij}^{Ku}(\mathbf{x},\mathbf{x}') + A^{u}\phi\delta_{ij} + B^{u}(\delta_{i3}\delta_{jk} - \delta_{ik}\delta_{j3})\alpha_{,k}^{u} \\ & - D^{u}\psi_{,ij}^{u} - x_3F^{u}\alpha_{,ij}^{u} - (G^{u}+B^{u})Q_I\beta_{,ji}^{u} \end{aligned} \tag{3}$$

where, $G_{ij}^{Ku}(\mathbf{x},\mathbf{x}') = \delta_{ij}\phi - \frac{\psi_{,ij}}{4(1-\nu')}$ is the Kelvin's solution multiplied by $4\pi\mu'$; $\psi = |\mathbf{x}-\mathbf{x}'|$ is the norm of Galerkin vector and $\phi = \frac{1}{\psi}$; $\mathbf{Q} = (1, 1, -1)$ is created for image source with respect to interface S and dummy index merely works for lower case letter following Mura's index notation [53]; the superscript u stands for cases when source point $\mathbf{x}'$ is located in the upper phase; $A^{u}, B^{u}, C^{u}, D^{u}, F^{u}$

and G^u are coefficients associated with elastic constants of two material as shown in Eq.(4) with the source in the upper phase,

$$\begin{aligned} A^u &= \frac{\mu' - \mu''}{\mu' + \mu''}, \quad B^u = \frac{2\mu'(1-2\nu')(\mu' - \mu'')}{(\mu' + \mu'')(\mu' + \mu''(3-4\nu'))} \\ C^u &= \frac{\mu' - \mu''}{2(1-\nu')(\mu' + (3-4\nu')\mu'')}, \quad D^u = \frac{3-4\nu'}{2}C \\ F^u &= \frac{2\mu'(\mu'(1-2\nu'') - \mu''(1-2\nu'))}{(\mu' + \mu''(3-4\nu'))(\mu'' + \mu'(3-4\nu''))} \\ G^u &= \frac{\mu'(\mu''(1-2\nu'')(3-4\nu') - \mu'(1-2\nu')(3-4\nu''))}{(\mu' + \mu''(3-4\nu'))(\mu'' + \mu'(3-4\nu''))} \end{aligned} \tag{4}$$

Other components are exhibited in Eq.(5) with $(\bar{*})$ standing for image sources,

$$\begin{aligned} \alpha^u &= \ln[x_3' - x_3 + \psi], \quad \overline{\alpha}^u = \ln[x_3' + x_3 + \overline{\psi}] \\ \beta^u &= (x_3' - x_3)\alpha^u - \psi, \quad \overline{\beta}^u = (x_3' + x_3)\overline{\alpha}^u - \overline{\psi} \end{aligned} \tag{5}$$

where α and β can be interpreted as definite integral along the third axis of ϕ and α within the range $[x_3, \infty]$, respectively, which are also known as Bousinesq's potential functions. To derive the fundamental solutions with source point located in the lower phase, one can follow [18] and [21] but switch the coordinates and material phases. Alternatively, given Eqs.(2) and (3), the method of symmetry can serve as a straightforward tool.

The fundamental solution satisfies the reciprocal properties shown in Eq. (6). Obviously, when the source point is located in the lower phase, the fundamental solution must keep the same form as Eqs.(2) and (3), however, some signs and terms need to be changed accordingly.

$$G_{ij}(\mathbf{x}, \mathbf{x}') = G_{ij}(\mathbf{x}', \mathbf{x}) \quad i \neq 3 \text{ or } j \neq 3, \quad G_{ij}(\mathbf{x}, \mathbf{x}') = G_{ji}(\mathbf{x}, \mathbf{x}'), \quad \text{otherwise} \tag{6}$$

Now, consider two pairs of field and source points, (i) $\mathbf{x}$ and $\mathbf{x}'$;(ii) $\mathbf{xp}$ and $\mathbf{xp}'$, where $\mathbf{xp} = -\mathbf{x}$ and $\mathbf{xp}' = -\mathbf{x}'$. In (i) and (ii), the material phases switch. Due to the reciprocal and symmetric mechanical properties, two fundamental solutions satisfy Eq. (7).

$$G_{ij}^u(\mathbf{x}, \mathbf{x}', \mathcal{C}', \mathcal{C}'') = G_{ij}^l(\mathbf{xp}, \mathbf{xp}', \mathcal{C}'', \mathcal{C}') \tag{7}$$

where the superscripts u and l represent the cases of the source point located at the upper and lower phases. When switching two phases of materials, the material coefficients change in Eq.(4)

that A^l and A^u are equivalent in this case. Because the fundamental solutions are in the same form, some components and signs change with negative sign accordingly, and the explicit form of $G^l_{ij}(\mathbf{x},\mathbf{x}')$ is shown as follows:

(3) when $x_3 > 0$ and $x'_3 < 0$

$$\begin{aligned} 4\pi\mu'' G^l_{ij}(\mathbf{x},\mathbf{x}') = G^{Kl}_{ij}(\mathbf{x},\mathbf{x}') + A^l\phi\delta_{ij} - B^l(\delta_{i3}\delta_{jk} - \delta_{j3}\delta_{ik})\alpha^l_{,k} \\ - D^l\psi_{,ij} + x_3 F\alpha^l_{,ij} - (G^l + B^l)Q_I\beta^l_{,ji} \end{aligned} \tag{8}$$

(4) when $x_3 < 0$ and $x'_3 < 0$

$$\begin{aligned} 4\pi\mu'' G^1_{ij}(\mathbf{x},\mathbf{x}') = G^{Kl}_{ij}(\mathbf{x},\mathbf{x}') + A^l\overline{\phi}\delta_{ij} - B^l(\delta_{i3}\delta_{jk} - \delta_{ik}\delta_{j3})\overline{\alpha}^l_{,k} \\ - C^l x_3\left[Q_J\overline{\psi}_{,ij3} + 4(1-\nu'')\delta_{j3}\overline{\phi}_{,i} + 2(1-2\nu'')\delta_{i3}Q_J\overline{\phi}_{,j} - Q_J x_3\overline{\phi}_{,ij}\right] \\ - D^l Q_I Q_J\overline{\psi}_{,ji} - (G^l + B^l)Q_J\overline{\beta}^l_{,ij} \end{aligned} \tag{9}$$

where $G^{Kl}_{ij}(\mathbf{x},\mathbf{x}') = \delta_{ij}\phi - \frac{\psi_{,ij}}{4(1-\nu'')}$; the coefficients $A^l - G^l$ can be obtained through switching the stiffness tensors in Eq.(4), for example, $A^l = \frac{\mu''-\mu'}{\mu''+\mu'}$. When $\mathcal{C}' = \mathcal{C}''$, all the coefficients $(A - G)$ become zero, hence, the fundamental solutions reduce to the Kelvin's solution for a homogeneous infinite domain with a point source. In addition, through adjusting the stiffness tensor of the upper or lower phase, the fundamental solution can be modified to several semi-infinite solutions, i.e the Mindlin's and Lorentz's problem [20]. α^l, β^l and their images are provided in Eq.(10),

$$\begin{aligned} \alpha^l = \ln[-x'_3 + x_3 + \psi], \quad \overline{\alpha}^l = \ln[-x'_3 - x_3 + \overline{\psi}] \\ \beta^l = (-x'_3 + x_3)\alpha^l - \psi, \quad \overline{\beta}^l = (-x'_3 - x_3)\overline{\alpha}^l - \overline{\psi} \end{aligned} \tag{10}$$

Comparing Eq.(5) with Eq.(10), the α and β functions are similar and their partial derivatives satisfy $\alpha^u_{,i} = -\alpha^l_{,i}$, $\alpha^u_{,ij} = \alpha^l_{,ij}$, and so does β.

3.2. Boundary integral equations

Consider the domain $\mathcal{D}$ shown in Fig.1 composed of two dissimilar isotropic subdomains $\mathcal{D}^+$ and $\mathcal{D}^-$ and $\mathcal{D}$ is subjected to prescribed boundary conditions of displacement $\mathbf{u}$ and surface traction $\mathbf{t}$. Given an arbitrary field point $\mathbf{x}$ within $\mathcal{D}$, using the Green's second identity and fundamental solution, the elastic fields can be obtained through the boundary integral equations (BIE) of Eq.(11),

$$u_i(\mathbf{x}) = -\int_{\partial\mathcal{D}^t} T_{ij}(\mathbf{x},\mathbf{x}')u_j(\mathbf{x}')d\mathbf{x}' + \int_{\partial\mathcal{D}^u} G_{ij}(\mathbf{x},\mathbf{x}')t_j(\mathbf{x}')d\mathbf{x}' \tag{11}$$

where $G_{ij}(\mathbf{x}, \mathbf{x}')$ is the fundamental solution of the displacement field in i^{th} direction with a unit concentrated force in the j^{th} direction shown in Eqs.(2),(3), (8), and (9) for the 4 cases of the positions of field and source points $\mathbf{x}$ and $\mathbf{x}'$ in the bi-material; $T_{ij}(\mathbf{x}, \mathbf{x}')$ is the fundamental solution of the traction in the i^{th} direction caused by a unit concentrated force in the j^{th} direction. $T_{ij}(\mathbf{x}, \mathbf{x}')$ can be expressed in terms of $G_{ij}(\mathbf{x}, \mathbf{x}')$ as follows,

$$T_{ij}(\mathbf{x}, \mathbf{x}') = \frac{\mathcal{C}_{imkl}(\mathbf{x}')(G_{kj,l'} + G_{lj,k'})}{2} n_m(\mathbf{x}') \tag{12}$$

Notice that one should use the stiffness tensor of source point, and the partial derivative is with respect to $\mathbf{x}'$, which are provided in Appendix A. To numerically solve the boundary value problem, one can discretize the boundary with elements and employ shape functions. Therefore, the BIE in Eq.(11) can be expressed in the discretized form [43]:

$$u_i(\mathbf{x}) = -\sum_{e=1}^{NE} H_{ij} u_j^e + \sum_{e=1}^{NE} U_{ij} t_j^e \tag{13}$$

where $H_{ij} = \int_{S_e} T_{mi}(\mathbf{x}, \mathbf{x}') N_{mj}(\mathbf{x}')\, dS$ and $U_{ij} = \int_{S_e} U_{mi}(\mathbf{x}, \mathbf{x}') N_{mj}(\mathbf{x}')\, dS$; NE is the number of elements; the superscript e represents nodal values of boundary displacements and surface tractions in the e^{th} element. After the discretized BIE is assembled into a global linear equation system, the boundary value problem can be solved numerically. Since the fundamental solution analytically consider the effect of interface S, it can solve bi-material system as a single domain, which is similar to solve a homogeneous elasticity problem.

The BEM with Kelvin's solution can also be applied to solve bi-material structures, it requires the discretization of the interface S and treats the problem with a multi-region scheme. In such case, more degrees of freedom are introduced to the system of linear equations and attention must be paid to control mesh quality of the interface. In one hand, multi-region scheme have higher computational demand due to the increase in the size of the global matrix; on the other hand, due to the singularity along the interface of a bi-material structure with thin film, much more efforts are required to ensure numerical stability and robustness in the solving process. Therefore, the BEM with bi-material fundamental solutions demands less computational resources and simplifies the simulation process. Besides the common bi-material structure, it can be directly applied to simulate effects of semi-infinite boundary, i.e, zero surface tractions, displacements, etc. The explicit form of fundamental solution can be used for particulate composites with bi-material matrix by

the recently-developed inclusion-based boundary element method as well [20, 54]. Since the single domain algorithm is based on BIEs of bi-material fundamental solution, it can be straightforwardly extended to other type of fundamental solutions, such as the Green's functions for transversely isotropic [23] and anisotropic [55] bi-materials. However, because those Green's functions are provided in integral form, high computational costs are expected, which can also be found in Yue's work for multi-layered solids [34]. Particularly, when tri-material systems exhibit a symmetric configuration including both loading conditions and material properties with respect to the mid-plane, they can be solved with the present bi-material solution by using the symmetric boundary conditions.

4. Numerical verification of BEM with bi-material fundamental solution

In this Section, the verification and validation are conducted by comparing the elastic fields from the proposed method with those from Finite Element Method, which was performed with ANSYS. Shown in Fig.2, the boundary conditions are set as, (i) the top surface of $\mathcal{D}^+$ is subjected to downward pressure 10KPa; (ii) the bottom surface of $\mathcal{D}^-$ completely restrained with zero allowable displacements; (iii) all other surfaces are free of traction. The width b, length l, and thicknesses T_1 and T_2 are all chosen as 1m. Two material properties are selected as, $\mu' = 4 \times 10^5$Pa, $\nu' = 0.25$ and $\mu'' = 8 \times 10^5$Pa, $\nu'' = 0.1$ for verification purposes. Effects of the thickness and stiffness tensor will be investigated subsequently with more case studies.

In Fig. 3, the variation of displacement components u_3 is exhibited within the range of $x_3 \in [-1, 1]$m along the vertical center line. Due to the constraints on the bottom surface of $\mathcal{D}^-$, the variation of u_3 is relatively smaller compared to that of field points in $\mathcal{D}^+$. When the field point is on the interface S, though u_3 is continuous, a sudden change of its slope is observed, which results in the discontinuity of stresses in Fig. 4(a). Regarding the convergence of BEM, three cases of boundary element mesh are considered, $90, 250$ and 1000; for FEM, $250,000$ elements are applied for reliable analysis. For the comparison in displacements, all three cases of BEM agree well with FEM although a minor improvement is observed with more refined boundary element mesh. However, when field point is close to the upper surface, cases (BEM (90) and BEM (250)) have jump points. Such phenomenon is caused by larger elements and insufficiently accurate Gauss quadrature because the distance to the boundary element is too close. As shown in case (BEM (1000)), the refined mesh can improve numerical stability in the post-process and 16-points Gauss quadrature are used.

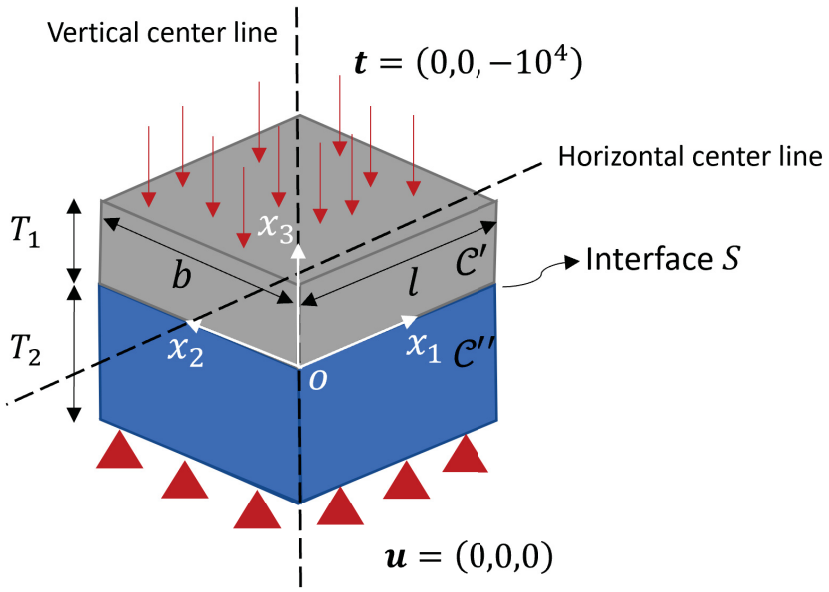

Figure 2: Geometry and boundary conditions for a bi-material structure $\mathcal{D}$ with two dissimilar layers with thickness T_1 and T_2, respectively

In Fig.4, there are some discrepancies among BEM(90), BEM(250) with FEM, particularly at the first and last points. It can be interpreted by the fact that stress field is a combination of partial derivatives of the displacement field. Hence, the variation becomes more rapid, which requires more elements to describe the actual behavior. In Fig. 4(b), the σ_{33} is continuous over the interface S, which satisfies the continuity conditions in Eq. (1). Except the last and beginning points, the maximum discrepancies between (i) BEM(90) and FEM is 0.99%; (ii)BEM(250) and FEM is 0.41%; (iii) BEM(1000) and FEM is less than 0.13%. For industrial applications, the single domain BEM could provide efficient and reliable analysis using 250 elements for the above case studies.

Fig. 5 shows the comparison of displacement u_3 ,normal stress σ_{33} and τ_{13} along the horizontal center line with $x_1 \in [-1, 1]$m, where the BEM(1000) case agrees well with FEM, except the two end points and shear stress. Notice that the curves of BEM(1000) exhibits larger discrepancy in field trends at end points, which indicates the numerical errors arisen by small ratio of distance and characteristic length of the element, which can be improved through more refine mesh or more accurate Gauss quadrature. In BEM [43], the displacement and stresses on the boundary can be calculated similarly as FEM that shape functions are applied to interpolate. In Fig. 5, the variation of normal stress τ_{31} on the interface S were plotted and the results from BEM with $90, 250, 1000$ and $16,000$ elements and FEM with $250,000$ elements were compared. A very good agreement

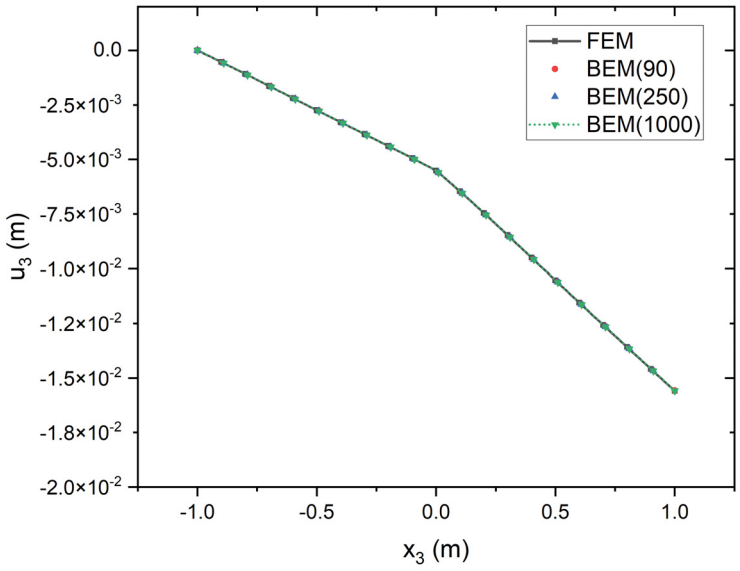

Figure 3: Comparison and variation of displacement u_3 under downward uniform pressure $10KPa$ along vertical center line within range $x_3 \in [-1, 1]m$

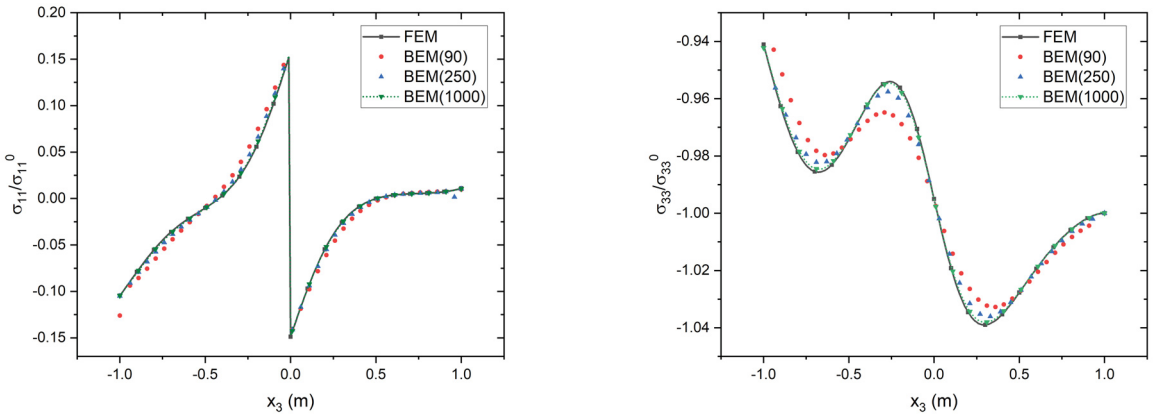

(a) σ_{11} (b) σ_{33}

Figure 4: Comparison and variation of normal stress (a) σ_{11}; (b) σ_{33} under downward uniform pressure $10kPa$ along vertical center line within range $x_3 \in [-1, 1]m$

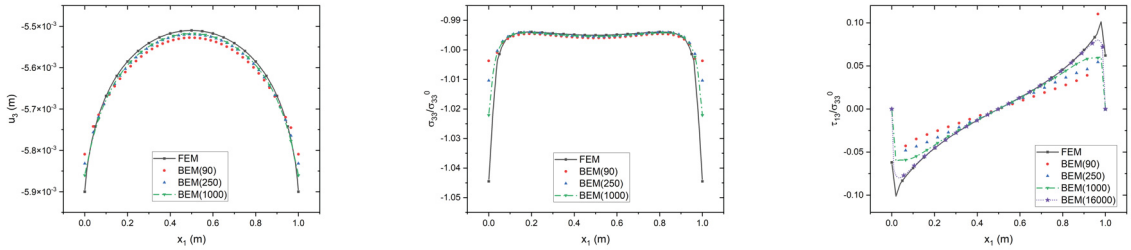

(a) u_3 (b) σ_{33} (c) $\tau 13$

Figure 5: Comparison and variation of (a) displacement u_3; (b) normal stress σ_{33}; (c) shear stress τ_{13} under downward uniform pressure $10kPa$ along horizontal center line on interface S within range $x_1 \in [-1, 1]m$

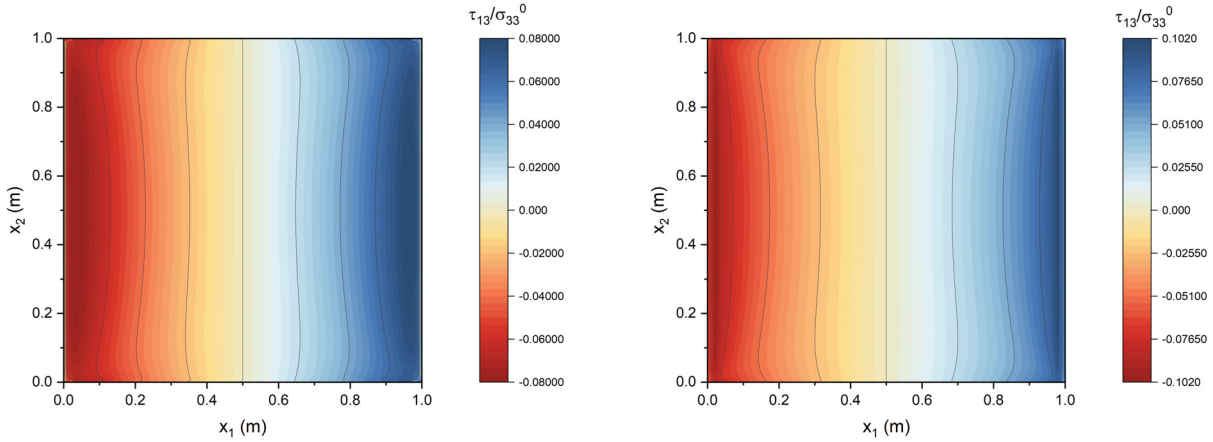

(a) BEM(1000) (b) FEM

Figure 6: Comparison of contour plot between BEM(1000) and FEM of $\tau 13$ on the interface S of the range $x_1 \in [0, 1]m$ and $x_2 \in [0, 1]m$ under uniform downward pressure $10KPa$

can be observed, except at the neighborhood of end-points. Due to the traction free boundary on the side surfaces, the shear stress there must be zero. However, the solution of FEM exhibits a non-zero value with a non-smooth curve around the end-points. Notice that the stress contour plot in Fig.6(a) is generated by 101×101 uniformly distributed points, while Fig. 6(b) used the element average method. Although the stress contour plots exhibit discrepancies as the range of the color bar, the major difference lies in the boundary as indicated by Fig. 5(c). The shear stress of boundary in FEM plot ($x_1 = 0$ and $x_1 = 1$) are not zero, which is indeed not accurate. For other positions, the two stress contour plots agree well with each other.

5. Applications to bi-material structures of wind turbines and solar panel

This section aims to analyze the elastic behavior of two common bi-material structures, a turbine blade under shearing loads and a solar panel under temperature loads. In general, due to the mismatch of material properties of $\mathcal{D}^+$ and $\mathcal{D}^-$, interfacial debonding is a commonly reason for the failure of the material systems. In the following, the variation of traction in the interface S and stress distribution along x_3 (thickness) direction will be investigated.

5.1. Case study of wind turbine blades

Considering a wind turbine blade, it is designed to sustain torsional load caused by air flows. Shown in Fig. 7, the wind turbine are mainly composed by fiber reinforced plastic (FRP) and Balsa/Foam according to the specific structure, covered with coating layer [56]. Specifically, around the trailing edge of the wind turbine, only FRP layer and coating layer are exited, and the fibers are usually placed along different directions in the adjacent FRP layers, such as (+45/-45) for bi-directions, which leads this kind of FRP possessing the same properties such as tensile modulus and compression modulus along both 0 and 90 directions. In order to simplify the simulation, we treat the FRP as the isotropic substrate. The thickness of the substrate varies around the trailing edge, with the same coating layer. Then, the skin of the blade can be simplified as a bi-material structure as shown in Fig. 7 (right side). Without the loss of any generality, (i) T_1 and T_2 are set as 1mm and 20mm [56], respectively; (ii) the width b and length l are selected as 100 mm; (iii) the material properties are set as, $\mu' = 1\,\text{GPa}, \nu' = 0.3$ and $\mu'' = 6.65\,\text{GPa}, \nu'' = 0.3$. The upper phase is subjected to pressure $(-20, 0, 0)\,\text{MPa}$ in the horizontal plane, which is equivalent to 1KN.m torque. To simulate the blade, 5 seeds are chosen to mesh x_3 (thickness) direction of $\mathcal{D}^+$, and the boundary mesh contains 5468 quadrilateral elements.

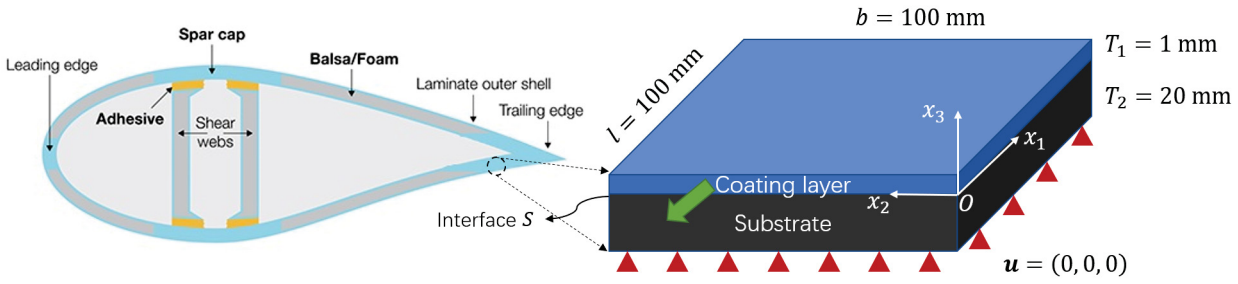

Figure 7: Schematic plot of wind turbine blade layer under pressure along x_1 direction

Fig. 8 shows the variation of elastic fields along the horizontal center line of the interface S. The pressure is applied on the surface $x_1 = 0$, the displacements and stresses decay rapidly when

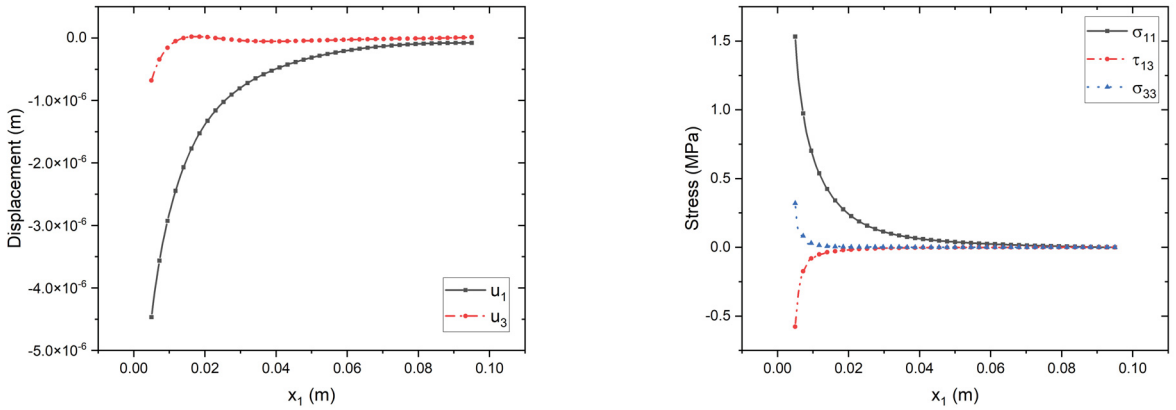

(a) (b)

Figure 8: Variation of elastic fields of wind turbine blade (a) displacement and (b) stress, under horizontal pressure 20MPa along the horizontal center line $x_1 \in [0.005, 0.095]$m

field points moves towards $x_1 = 0.1$m. Notice that, compared with u_1 and u_3, u_2 is a small quantity (approximately 10^{-2} of u_3), hence it was not plotted in Fig. 8(a). Regarding to displacement fields, the dominate deformation exists in x_1 direction, which results in the larger normal stress σ_{11}. In Fig. 8 (b), the direction of normal stresses are positive while that of shear stress is negative, which can be interpreted that in addition to σ_{11}, τ_{13} is involved in resisting the shearing loads. Comparing among the three stresses, σ_{11} and τ_{13} are the dominant ones.

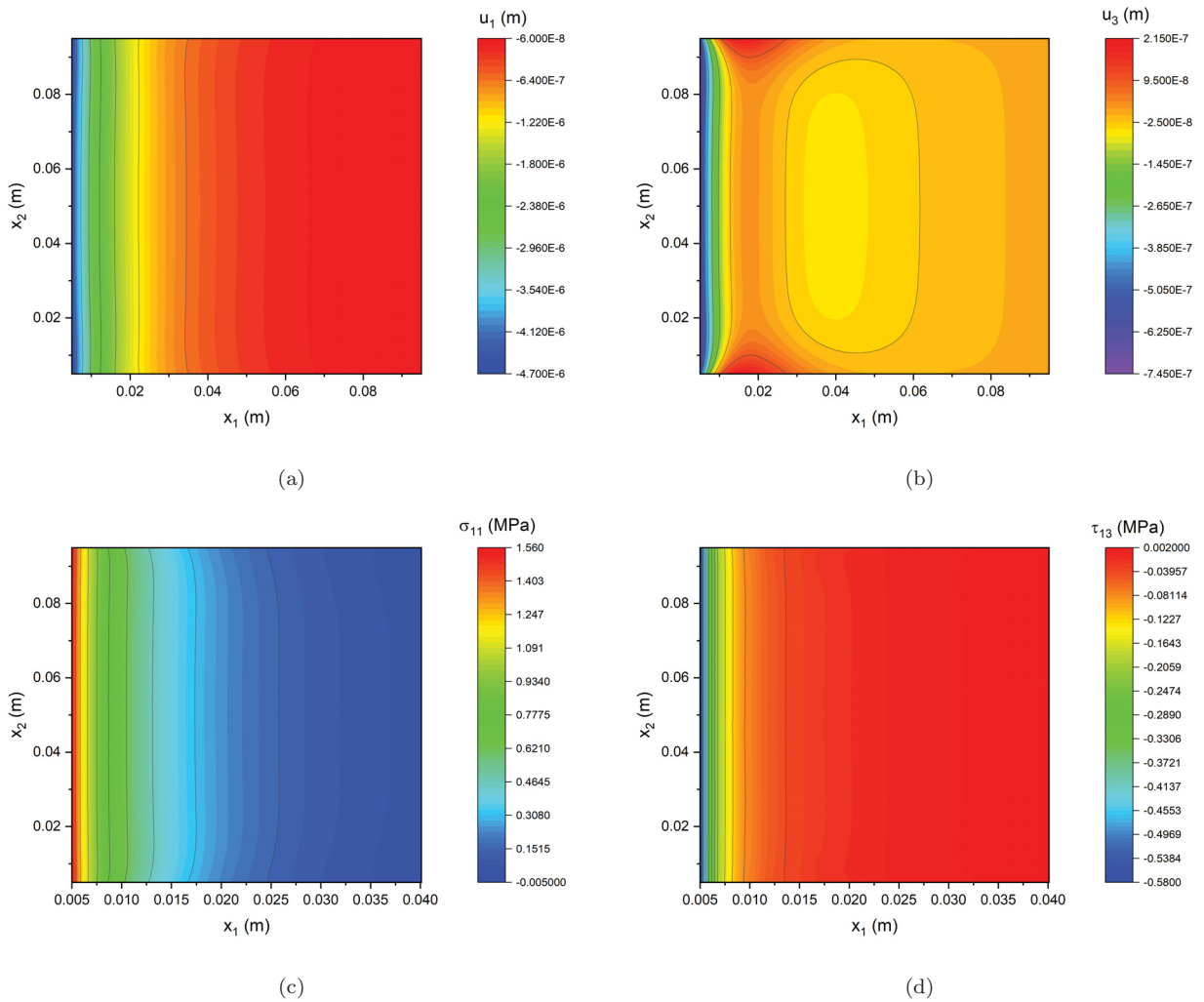

Figure 9: Contour plots of elastic fields of wind turbine blade (a) u_1, (b) u_3, (c) σ_{11} and (d) τ_{13} under horizontal pressure 20MPa within range $x_1 \in [0.005, 0.04]$m and $x_2 \in [0.005, 0.095]$m

In Fig. 9, the elastic fields of interface S are presented by contour plots. Regarding the displacements, the contour levels in Fig.9(a) are observed more uniform compared with Fig.9(b) that u_1 of interface S is completely negative. However, as for u_3, though negative in the entering part, it is positive around the boundary in x_2 direction (shown in red). Especially, the two red regions (close to $x_1 = 0.02$) in Fig. 9(b) indicates there is warpage due to the shear loads. As shown in Fig.8(b), stress fields decay rapidly, hence, only areas with $x_1 < 0.04$m are considered. Similar to displacements, the variation of σ_{11} and τ_{13} along x_2 direction are comparatively small, which can be interpreted that although τ_{13} is a combination of derivatives of u_1 and u_3, u_1 is the dominate one.

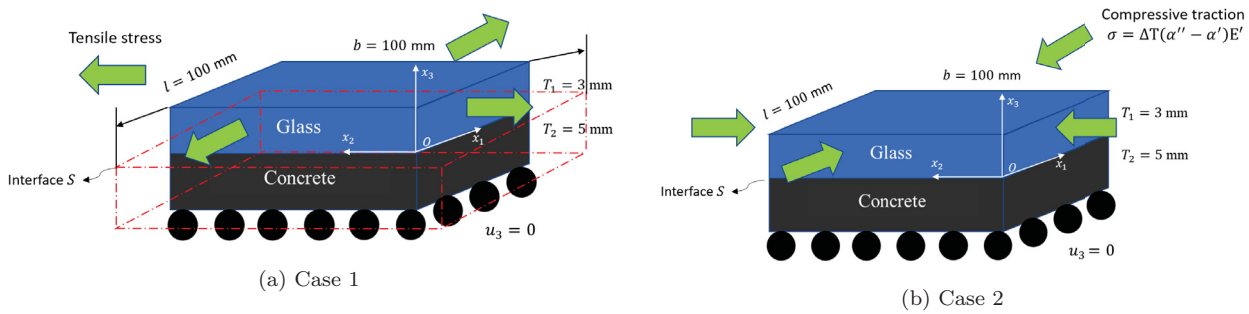

(a) Case 1

(b) Case 2

Figure 10: Schematic plot of two superposed cases to simulate thermal-mechanical problem of a solar panel

5.2. Case study of solar panels

Solar panels can be installed onto the roof to harvest solar energy to minimize conventional energy consumption and potential pollution. It is indeed a bi-material system, a glass layer bonded to a concrete substrate, and then rests on a laminated roof panel. Solar panels experience large temperature changing. Meanwhile, the thermal expansion coefficient of concrete substrate (α'') is much larger than that of glass overlay (α'), resulting a mismatch in deformation upon thermal loading. Intuitively speaking, this mismatch will result in tensile stress in glass overlay, thereby potentially causing cracks and leading to improper functioning. However, the exact stress distribution is complicated so that numerical methods are required for an accurate prediction. In this case study, we demonstrate our algorithm suffices to predict the stress field under thermal loading. The present algorithm assumes the uniform temperature variation of solar panels under the extreme temperature events. In actual application, the thermal gradient across the thickness of solar panels changes with the temperature difference between the two surfaces as well as solar irradiation over time, the thermal stress state will be more complicated. A typical way is to implement the domain integrals of temperature variation and partial derivatives of Green's function $G_{ij,j'}$. Following Gao's work [57] on the radial integral method, for some simple distribution of temperature (uniform, linear, quadratic, etc), the domain integrals can be conducted without internal cells. However, domain integrals cannot be avoided for complicated temperature variations. Alternatively, Prasad et al. [58] transformed the domain integral into boundary surface integrals through Green's second identity, thus the merits of BEM without interior discretization are retained and the extension of this method to thermoelastic problem is underway.

To alleviate the strong thermal effects in substrates, the laminated roof is designed to provide vertical support to the solar panel ($u_3 = 0$) so the horizontal degrees of freedom (u_1 and u_2) at the bottom surface of our model are released. As an industrial application, according to [59], (i) T_1

and T_2 are set as 3mm and 5mm; (ii) the width b and length l are set as 100mm; (iii) the material properties of glass and concrete are $E' = 72\text{GPa}$, $\nu' = 0.2$, $\alpha' = 6\times10^{-6}/°\text{C}$, $E'' = 36\text{GPa}$, $\nu'' = 0.2$, $\alpha'' = 1.1\times10^{-5}/°\text{C}$; (iv) the temperature change is selected as $\Delta T = 50°\text{C}$. Although the thermal-mechanical problems can be simulated using volume integrals of inelastic strains, alternatively, in this section, the problem is decomposed into two cases [60]. In case 1, the glass and concrete layers extends freely, and uniform tensile stress ($\sigma_{11} = \sigma_{22}$) is applied to the glass layer to stretch it to match the extension of concrete. In case 2, compressive tractions, $T_n = \Delta T(\alpha'' - \alpha')E' = 22.5\text{MPa}$ (n refers to normal direction of the surface), are applied to the side edges of glass, which forms a well-defined boundary value problem, which is demonstrated in Fig. 10. To simulate the solar panel, 8200 boundary elements were used.

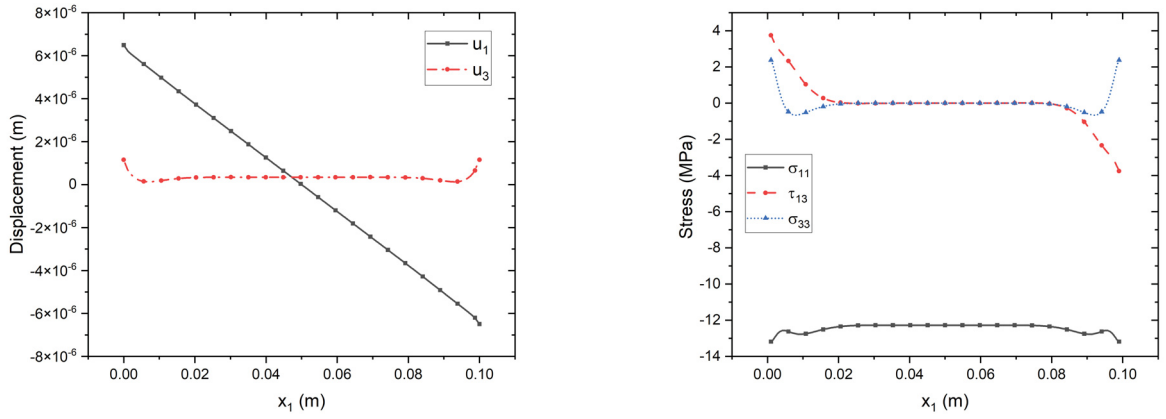

(a) (b)

Figure 11: Variation of elastic fields of solar panel (a) displacement and (b) stress, under thermal load along the horizontal center line $x_1 \in [0.001, 0.099]m$

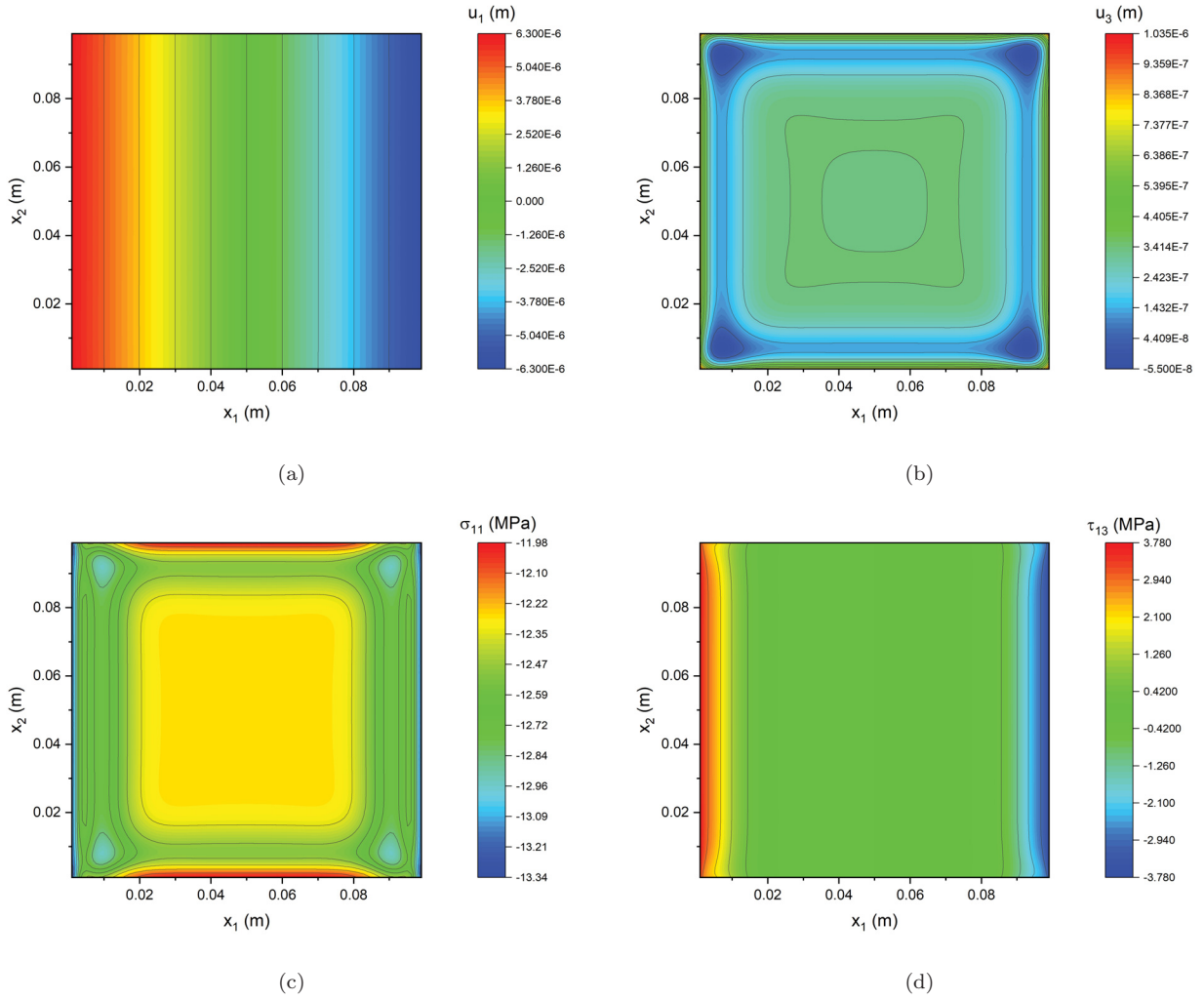

Figure 12: Contour plots of elastic fields of solar panel (a) u_1, (b) u_3, (c) σ_{11} and (d) τ_{13} under thermal load within range $x_1 \in [0.001, 0.099]m$ and $x_2 \in [0.001, 0.099]m$

Fig. 11(a) shows the variation of u_1 and u_3 along the horizontal center line. In the interior region of the model, u_1 demonstrates a linear anti-symmetric trend with 0 value at the center, while u_3 has comparatively smaller variation over the interface. These two tendencies proves that the glass overlay is uniformly stretched along horizontal directions in this region. To the contrast, in the neighborhood of edges, u_1 curve tilts up, which can be interpreted that the actual displacement is smaller than that it is supposed to be if the uniform stretching was preserved. Moreover, u_3 becomes positive in this region. At the free edge, because of the thermal strain mismatch, the glass overlay has the tendency to pull up the concrete substrate and the glass itself is squeezed to some extent as well. This phenomenon itself explains the displacement variation. The stress plot in Fig. 11(b) agrees well with our finding. In the interior region, σ_{11} keeps a constant value, and both τ_{13}

and σ_{33} are 0. Because of the uplifting of concrete near the edge, the non-zero τ_{13} and σ_{33} values concentrate in these regions. Interestingly, the magnitude of σ_{11} jumps near the edge, and it can be explained by equilibrium conditions. For an infinitesimal element near the edge, the non-zero τ_{13} is balanced by the integration of σ_{11} along the vertical direction, thereby causing the increase in the magnitude of σ_{11}.

Fig. 12(a) and (b) are the contour plots of u_1 and u_3 along the horizontal interface between two materials. u_1 value is independent from x_2 coordinate because of no constraint along x_2 direction. Both x_1 and x_2 directions are equivalent for u_3, so the distribution patterns along the 4 edges are identical and u_3 at the four corners are doubled. Fig. 12(c) and (d) are the stress contour plots. Obviously, τ_{13} is not related to x_2. Along the x_2 direction, the trend of σ_{11} observed on Fig. 11(b) only applies to the middle region, while at the edge, σ_{11} increases and decreases to its minimum value at the edge. This is because σ_{11} needs to balance σ_{21}, which concentrates near the edge but is 0 at the free edge.

6. Parametric study of ratio of thickness and shear modulus in elastic fields

In Section 5, the variations of elastic fields of wind turbine blades and solar panel under various boundary conditions were investigated. In these two applications, the ratios of thickness were selected based upon industrial applications and the results suggest that the ratio of thickness play important roles in the elastic fields. In general, when the ratio of thickness decreases, the upper layer become more fragile to the shearing effects. In addition, the difference of stiffness tensors may also affect the elastic fields as well. Although the stiffness tensor is composed of shear modulus and Poisson's ratio, parametric studies focus on the dominant one, the ratio of shear modulus. Shown in Fig. 2, the width b, length l and T_2 are set as 1m and the bottom surface of $\mathcal{D}^-$ remains completely constrained. Other boundary conditions and geometric dimension are specified in the subsections.

6.1. Effects of ratio of thickness

This subsection aims to investigate the effects brought by thickness ratio $\frac{T_1}{T_2}$ under two loading conditions, (i) uniform downward pressure $\mathbf{t} = (0, 0, -10^4)$Pa applied on top surface of $\mathcal{D}^+$ and all other surfaces are free of tracions; (ii) horizontal pressure applied $\mathbf{t} = (0, 0, -10^4)$Pa applied on front surface ($x_2 - x_3$ plane) of $\mathcal{D}^+$, and all other surfaces (except bottom surface) are free of traction. Five thickness ratios, $1, 0.5, 0.2, 0.1, 0.01$ are studied and the material properties remain

the same as Section 4. Notice that for case $\frac{T_1}{T_2} = 0.01$, because the thickness T_1 is thin enough, the elastic behaviors are similar to a structure with the lower phase $\mathcal{D}^-$ under boundary condition (i) (downward pressure). Therefore, only boundary condition (ii) is considered for such case. In this subsection, due to the change of thickness T_1, the displacement and stress fields are plotted either along vertical center line ($x_3 \in [-0.9, 0]$m) or horizontal center line of interface S ($x_1 \in [0.05, 0.95]$m) with 201 uniformly distributed field points. On the interface, because the normal stresses σ_{11} and σ_{22} are discontinuous, the normal stresses are selected from the bottom of the upper phase.

6.1.1. Downward pressure loads

Fig. 13, Fig.15(a) and Fig.15 (b) show the variation of u_3, σ_{11} and σ_{33} along the vertical center line, the results of the four cases are close, indicating that the change of thickness ratio has minor effect on the elastic field of the substrate under downward pressure loads. Subsequently, Fig.14 plots u_1 and u_3 along the horizontal center line of the interface S. Although the curves in Fig.14(a) exhibit some discrepancies, the difference is less than 4%, i.e between "ratio = 1" and "ratio = 0.1". In Fig.14 (b), when the thickness ratio decreases, the maximum u_3 decreases and the variation of u_3 increases. However, when ratio equals 0.1, the trend inverses. In such case, the elastic behavior of the upper phase transits from thick plate to thin plate, whose normal shearing deformation is small. Similar phenomenon can be observed in (c) and (d) of Fig. 15 that σ_{11} of case "ratio = 1" is obviously larger than other cases and the distribution of σ_{33} changes.

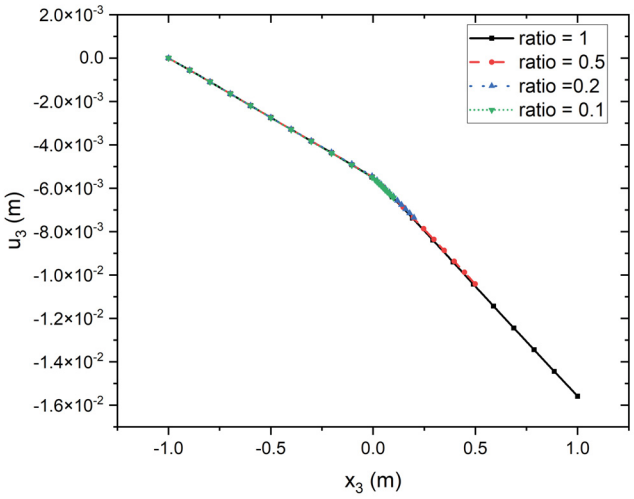

Figure 13: Variation of displacement u_3 under downward uniform pressure $10^4 Pa$ with thickness ratios $1, 0.5, 0.2$ and 0.1 along the vertical center line $x_3 \in [-0.9, 0.9]m$

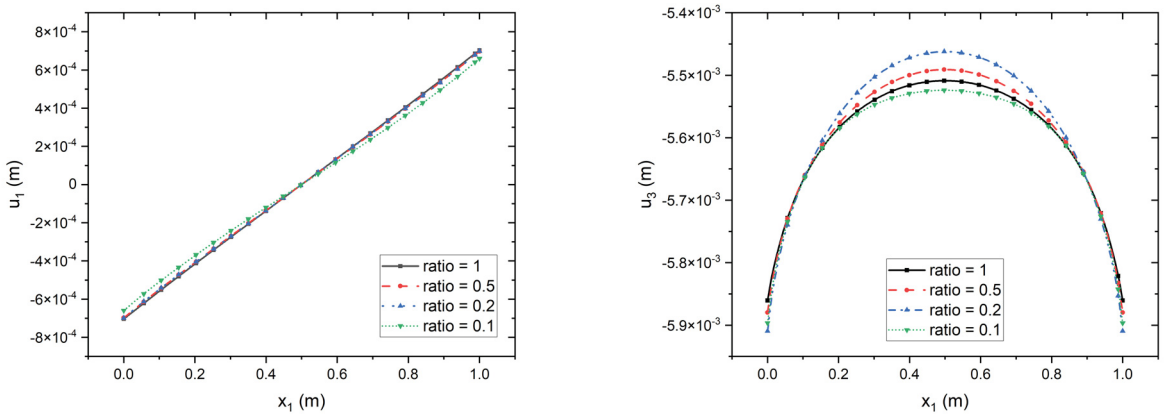

(a) (b)

Figure 14: Variation of displacement (a) u_1, (b) u_3 under downward uniform pressure $10^4 Pa$ with thickness ratios $1, 0.5, 0.2$ and 0.1 along the horizontal center line $x_1 \in [0.05, 0.95]m$

6.1.2. Horizontal pressure loads

The boundary condition (ii) specify a uniform horizontal pressure, because the applied force decreases with thickness ratio, which causes numerical results in different orders. Therefore, in this subsection, the elastic fields are normalized by the thickness ratio, i.e, $\overline{u}_1 = u_1 \frac{T_2}{T_1}$. Fig. 16 shows the variation of $\overline{u}_1$ and $\overline{u}_3$ along two center lines that when the thickness ratio decreases, $\overline{u}_1$ and $\overline{u}_3$ exhibit inverse trends. In addition to cases of downward pressure in Section. 6.1.1, the thickness ratio classifies "membrane"-like elastic behavior of case 0.01, where the uni-axial compression dominates. In Fig.16(c) and Fig.17(d), the case "ratio = 0.01" has the largest variation and maximum values of $\overline{u}_1$ and $\overline{\sigma}_{11}$ among other cases. Although the dominate load for case "ratio = 0.01" is the compression in x_1 direction, Fig. 16(d) indicates that the thin film bends to sustain deformations in x_3 direction to resist normal deformations generated by bottom constraint of the substrate. Besides normal stresses, shear stress τ_{13} in Fig. 17 increases significantly with smaller thickness ratios, which explains why the bonding layer of thin film bi-material structures is fragile under the shearing loads.

6.2. Effects of ratio of shear modulus

This subsection aims to investigate how ratios of shear modulus influence the bi-material structures. As indicated in Section. 5 and Section 6.1, the interface S becomes fragile when ratio of thickness is small because of the rapid increase of shear stress. Although bi-material structures with smaller thickness ratios arouse interests of strong shearing effects on the interface S, in this

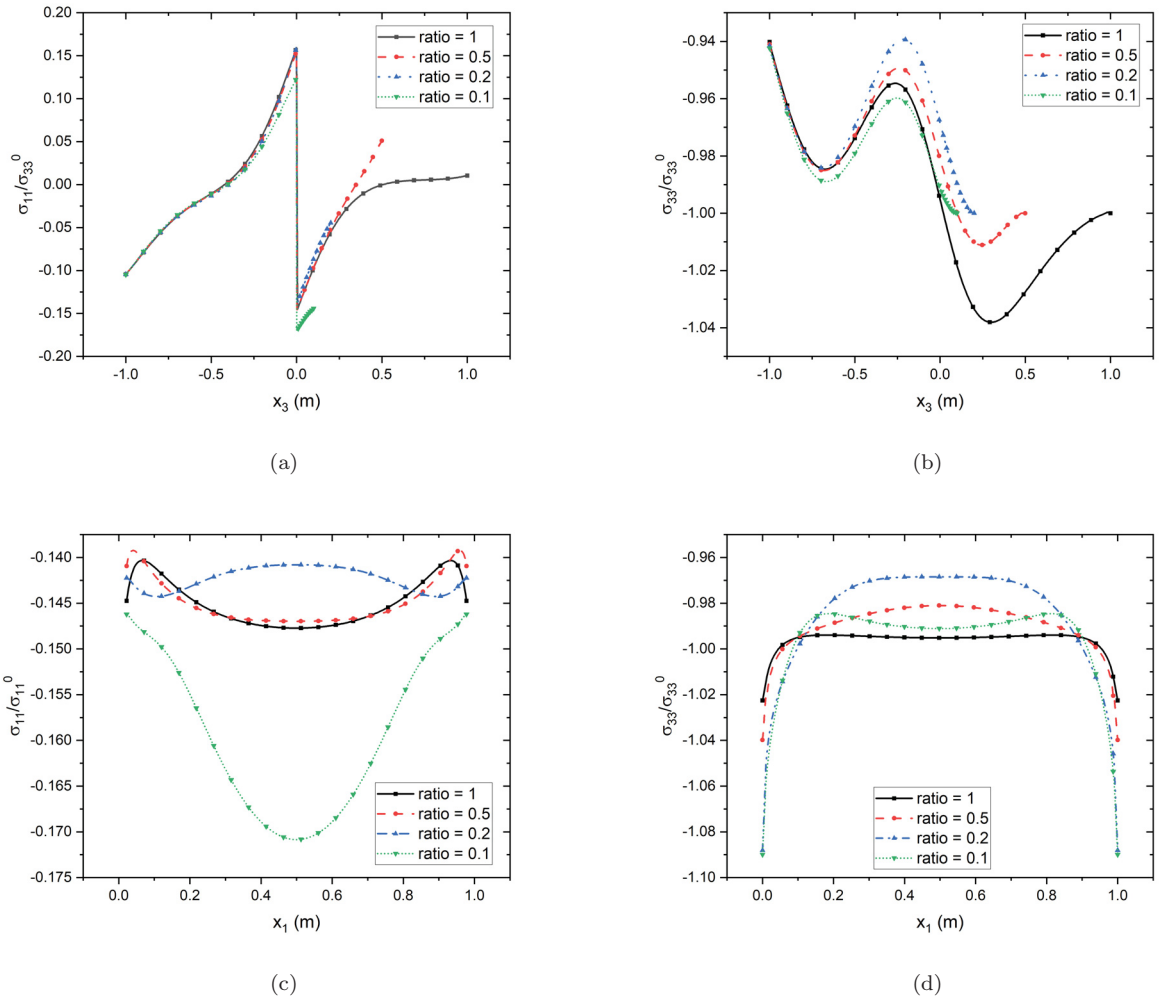

Figure 15: Variation of ratio of normal stress (a) $\sigma_{11}/\sigma^0_{33}$, (b) $\sigma_{33}/\sigma^0_{33}$ along the vertical center line; (c) $\sigma_{11}/\sigma^0_{33}$, (d) $\sigma_{33}/\sigma^0_{33}$ along the horizontal center line $x_1 \in [0.05, 0.95]m$ under downward uniform pressure $10^4 Pa$ with thickness ratios $1, 0.5, 0.2$ and 0.1

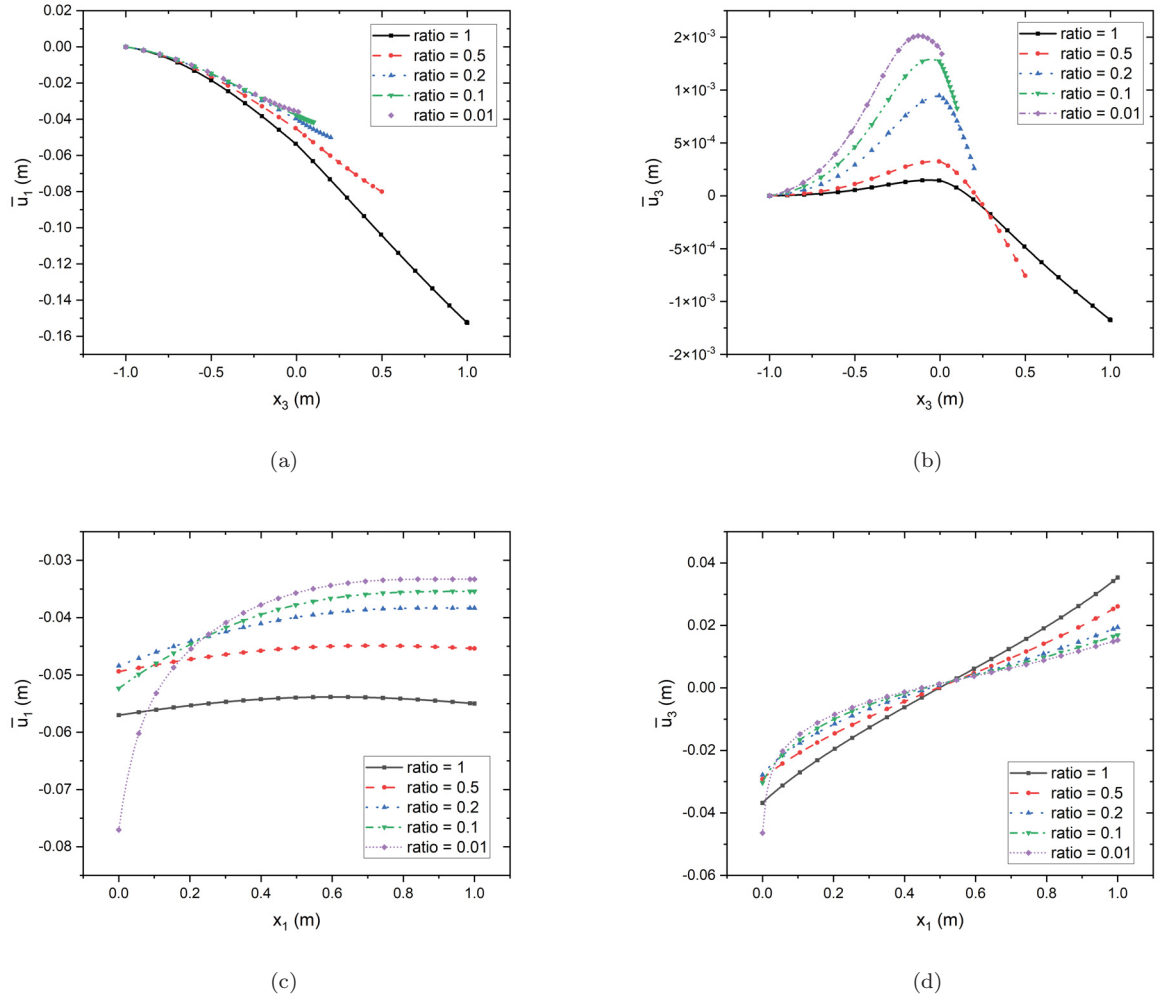

Figure 16: Variation of displacement (a) u_1, (b) u_3 along the vertical center line; (c) u_1, (d) u_3 along the horizontal center line $x_1 \in [0.05, 0.95]m$ under uniform horizontal pressure $10^4 Pa$ with thickness ratios $1, 0.5, 0.2, 0.1$ and 0.01

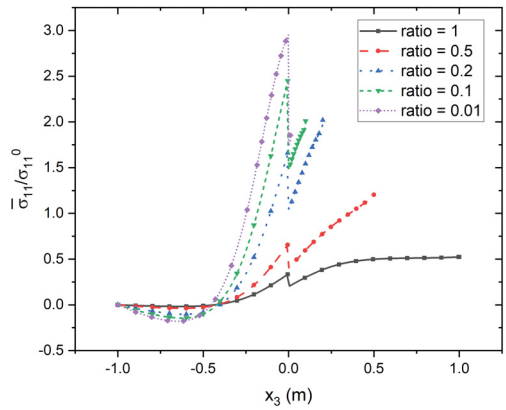

(a)

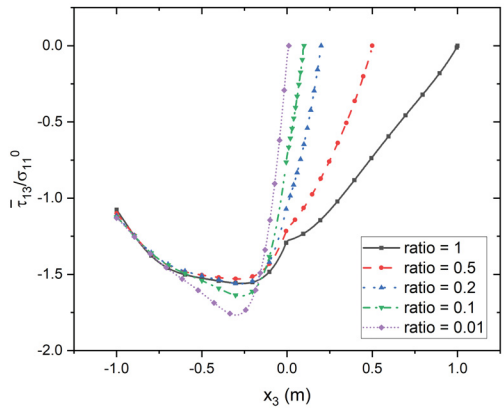

(b)

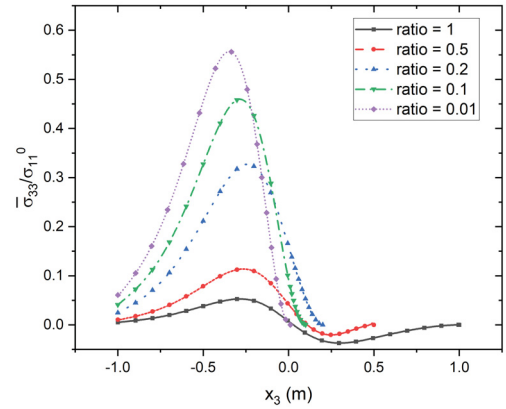

(c)

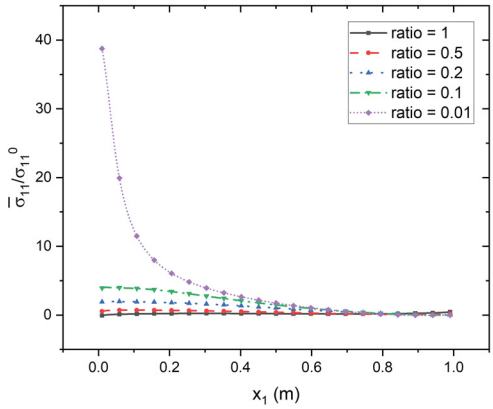

(d)

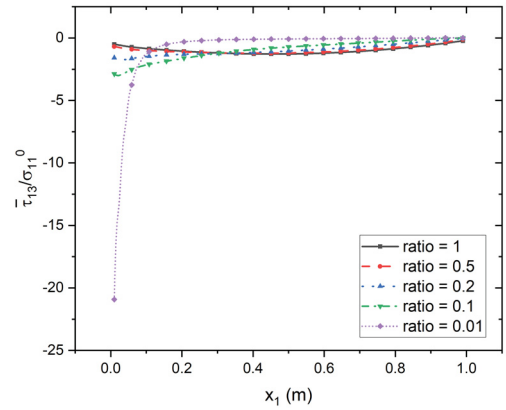

(e)

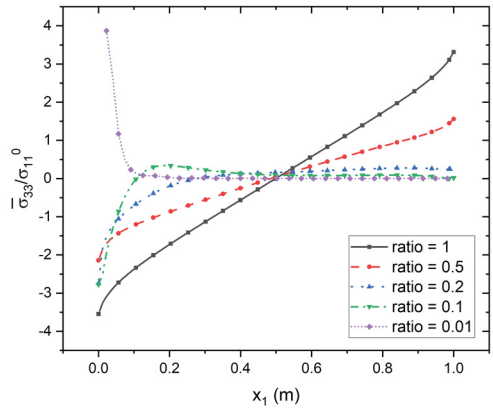

(f)

Figure 17: Variation of ratio of stresses (a) $\overline{\sigma}_{11}/\sigma_{11}^0$, (b) $\overline{\tau}_{13}/\sigma_{11}^0$, (c) $\overline{\sigma}_{33}/\sigma_{11}^0$ along the vertical center line; (d) $\overline{\sigma}_{11}/\sigma_{11}^0$, (e) $\overline{\tau}_{13}/\sigma_{11}^0$, (f) $\overline{\sigma}_{33}/\sigma_{11}^0$ along the horizontal center line $x_1 \in [0.05, 0.95]m$ under uniform horizontal pressure $10^4 Pa$ with thickness ratios $1, 0.5, 0.2, 0.1$ and 0.01

subsection, we intend to study bi-materials with more inclusive elastic behaviors, including both bending and shearing deformations. Hence, (i) the thickness ratio $\frac{T_1}{T_2} = 0.1$ is applied; (ii) five shear modulus ratios are considered: $\frac{\mu'}{\mu''} = 1, 2, 5, 10$ and 20 while the Poisson's ratio remain the same as Section. 4 ($\nu' = 0.25$, $\nu'' = 0.1$); (iii) boundary conditions are: horizontal pressure applied $\mathbf{t} = (0, 0, -10^4)Pa$ applied on front surface ($x_2 - x_3$ plane) of $\mathcal{D}^+$, and all other surfaces (except bottom surface) are free of traction. Fig. 18 exhibits the variation of displacement along the vertical and horizontal center lines. When the shear modulus ratio increases, the upper phase is stiffer so smaller deformations can resist the horizontal pressure loads. Hence, all displacement fields gradually decrease with increase of shear modulus ratio.

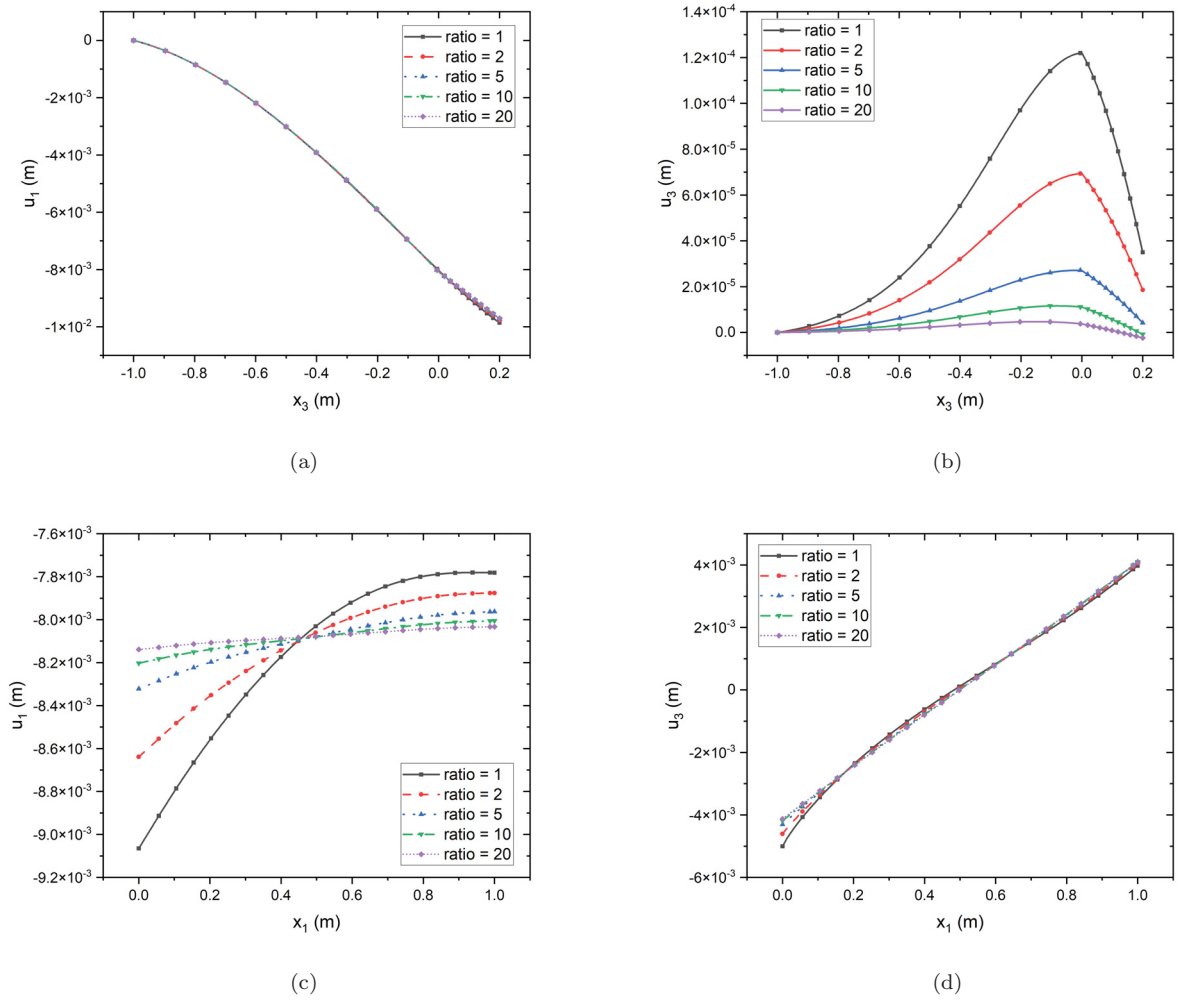

(a) (b)

(c) (d)

Figure 18: Variation of displacement (a) u_1, (b) u_3 along the vertical center line; (c) u_1, (d) u_3 along the horizontal center line $x_1 \in [0.05, 0.95]m$ under uniform horizontal pressure $10^4 Pa$ with ratios of shear modulus $1, 2, 5, 10$ and 20

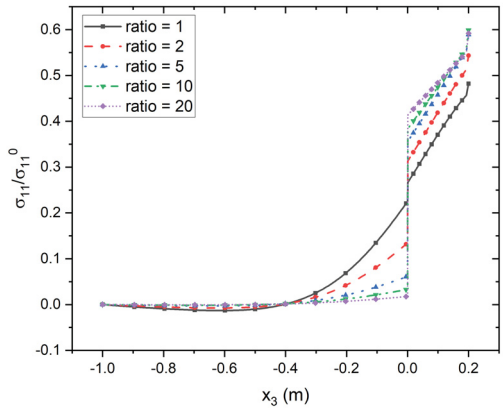

(a)

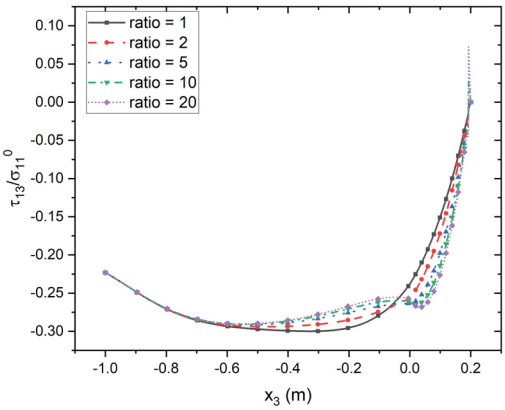

(b)

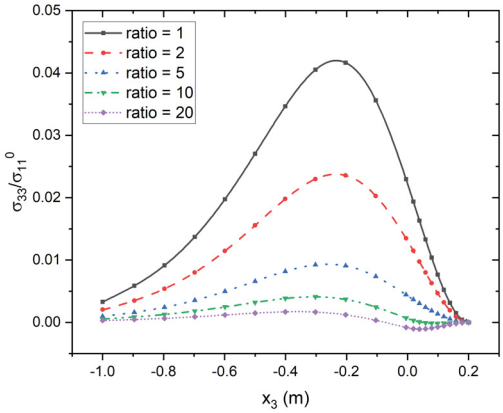

(c)

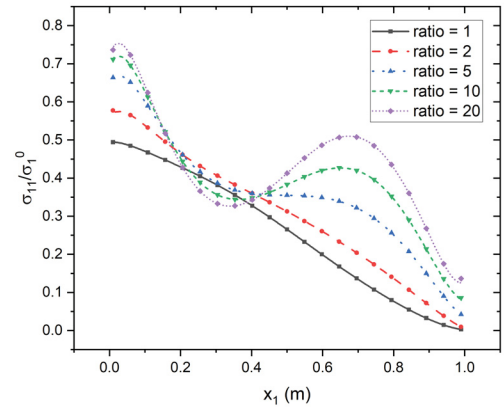

(d)

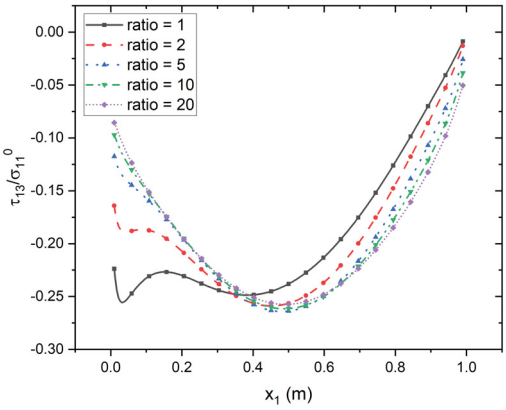

(e)

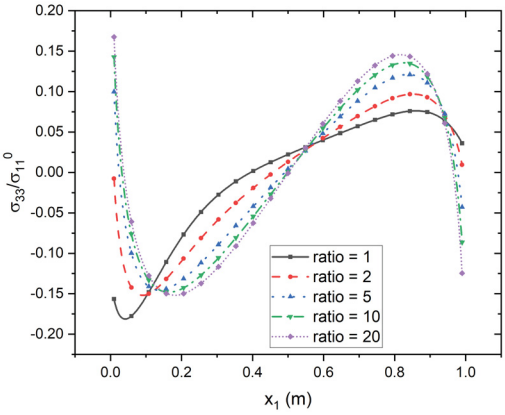

(f)

Figure 19: Variation of ratio of stresses (a) $\overline{\sigma}_{11}/\sigma^0_{11}$, (b) $\overline{\tau}_{13}/\sigma^0_{11}$, (c) $\overline{\sigma}_{33}/\sigma^0_{11}$ along the vertical center line; (d) $\overline{\sigma}_{11}/\sigma^0_{11}$, (e) $\overline{\tau}_{13}/\sigma^0_{11}$, (f) $\overline{\sigma}_{33}/\sigma^0_{11}$ along the horizontal center line $x_1 \in [0.05, 0.95]m$ under uniform horizontal pressure $10^4 Pa$ with shear modulus ratios as $1, 2, 5, 10$ and 20.

Fig. 19 illustrates the variation of $\bar{\sigma_{11}}$, $\bar{\sigma_{13}}$, $\bar{\sigma_{33}}$ along the vertical and horizontal directions under uniform horizontal pressure with respect to the shear modulus ratios of $1, 2, 5, 10$ and 20. Along the vertical direction, the shear modulus affects the stresses sharply when it is close to the interface. Meanwhile, $\bar{\sigma_{11}}$ and $\bar{\sigma_{13}}$ are larger than $\bar{\sigma_{33}}$, which dominate the mechanical behavior of bi-materials. Along the horizontal direction, the stress distribution is very sensitive to the shear modulus. When the shear modulus of each layer are close, say ratio 1 or 2, the stresses behave in a similar way. However, when the ratio is larger than 5, the stresses change significantly near the interface. Especially, $\bar{\sigma_{11}}$ is much larger than $\bar{\sigma_{13}}$ and $\bar{\sigma_{33}}$, and the stress curve is totally different when the ratio reaches to 20.

7. Conclusions

The algorithm of the single domain boundary element method, which was firstly presented in 1980s for 2D problems, has been implemented for 3D applications to investigate the elastic fields of bi-layered material systems. The method is verified with FEM through case studies of bi-material systems composed of two dissimilar cuboids. Thanks to the fundamental solution of bi-materrials, the single domain BEM calculates the elastic field of bi-layered material systems similarly to a homogeneous solid. The method is applied to investigate wind turbine blades under pressure load on the surface and solar panels under thermal loads and predicts the stress and deformation in the bi-layered material systems. The method is particularly suitable for the design and stress analysis of thin-film substrate systems. It exhibits the following advantages over the multi-domain BEM or FEM:

1. Without discretization of the interface, a few elements can provide high fidelity results for the bi-layered material systems.

2. The issues of discontinuity and singularity of the stress distribution are analytically treated, so that the program can provide convergent and robust prediction.

3. Excellent stability of the computation can be reached for a large range of the ratios of thickness, stiffness, and loading between the two layers.

The parametric studies demonstrate the versatile capability of this method to investigate the elastic behaviors of bi-material systems. The method can be extended to other applications, such as bi-layered Stokes' flow, heat conduction in bi-layered soilds, among other physical problems, by using the corresponding Green's function in the bi-layered material systems [19, 20].

Declaration of Competing Interest

No.

Acknowledgement

This work is sponsored by the National Science Foundation IIP #1738802, IIP #1941244, CMMI#1762891, U.S. Department of Agriculture NIFA #2021-67021-34201, and National Natural Science Foundation of China (Grant No. 12102458), whose support is gratefully acknowledged.

Appendix A. Partial derivatives of fundamental solutions

When the field point and source point are in the same phase ($x_3' x_3 > 0$), the fundamental solution contains both ordinary components and image components, whose partial derivatives changes in the third derivatives that, taking $\overline{\phi}$ as the instance,

$$\overline{\phi}_{,i'} = -Q_I \phi_{,i} \tag{A.1}$$

such chain rules apply to higher order partial derivatives as well. In order to derive the fundamental solution to tractions and conduct the post-process of stress field, first and second order partial derivatives are provided in the following. When $x_3' x_3 > 0$, the first order partial derivative (w.r.t x_k') is written as,

$$\begin{aligned} 4\pi\mu^p G^c_{ij,k'}(\mathbf{x},\mathbf{x}') = &(-\delta_{ij}\phi_{,k} + \frac{\psi_{,ijk}}{4(1-\nu^p)}) - A^c\delta_{ij}\overline{\phi}_{,k}Q_K - WB^c(\delta_{i3}\delta_{jm} - \delta_{im}\delta_{j3})Q_K\overline{\alpha}^c_{,mk} \\ &- C^c x_3\left[-Q_JQ_K\overline{\psi}_{,ij3k} - 4(1-\nu^p)\delta_{j3}Q_K\overline{\phi}_{,ik} - 2(1-2\nu^p)\delta_{i3}Q_JQ_K\overline{\phi}_{,jk} + x_3Q_JQ_K\overline{\phi}_{,ijk}\right] \\ &+ D^cQ_IQ_JQ_K\overline{\psi}_{,ijk} + (G^c+B^c)Q_JQ_K\overline{\beta}^c_{,ijk} \end{aligned} \tag{A.2}$$

and the second order partial derivatives (w.r.t x_k and x_l'),

$$\begin{aligned} 4\pi\mu^p G^c_{ij,kl'}(\mathbf{x},\mathbf{x}') = &(-\delta_{ij}\phi_{,kl} + \frac{\psi_{,ijkl}}{4(1-\nu^p)}) - A^c\delta_{ij}Q_L\overline{\phi}_{,kl} - WB^c(\delta_{i3}\delta_{jm} - \delta_{im}\delta_{j3})Q_L\overline{\alpha}^c_{,mkl} \\ &- C^c\delta_{k3}\left[-Q_JQ_L\overline{\psi}_{,ij3l} - 4(1-\nu^p)\delta_{j3}Q_L\overline{\phi}_{,il} - 2(1-2\nu^p)\delta_{i3}Q_JQ_L\overline{\phi}_{,jl} + x_3Q_JQ_L\overline{\phi}_{,ijl}\right] \\ &+ C^c x_3\Big[-Q_JQ_L\overline{\psi}_{,ij3kl} - 4(1-\nu^p)\delta_{j3}Q_L\overline{\phi}_{,ikl} - 2(1-2\nu^p)\delta_{i3}Q_JQ_L\overline{\phi}_{,jkl} \\ &+ x_3Q_JQ_L\overline{\phi}_{,ijkl} + \delta_{k3}Q_JQ_L\overline{\phi}_{,ijl}\Big] + D^cQ_IQ_JQ_L\overline{\psi}_{,ijkl} + (G^c+B^c)Q_JQ_L\overline{\beta}_{,ijkl} \end{aligned} \tag{A.3}$$

where the superscript $p = '$, $c = u$ when $x_3' > 0$ and $p = ''$, $c = l$ when $x_3' < 0$; $W = 1$ when $x_3' > 0$ and $W = -1$ when $x_3' < 0$. When the field point and source point are in different phases, the first order partial derivative is,

$$\begin{aligned} 4\pi\mu^p G^c_{ij,k'}(\mathbf{x},\mathbf{x}') = &(-\delta_{ij}\phi_{,k} + \frac{\psi_{,ijk}}{4(1-\nu^p)}) - A^c\delta_{ij}\phi_{,k} - WB^c(\delta_{i3}\delta_{jm} - \delta_{im}\delta_{j3})\alpha^c_{,mk} \\ &+ D^c\psi_{,ijk} + \chi x_3F^c\alpha^c_{,ijk} + (G^c+B^c)Q_I\beta_{,ijk} \end{aligned} \tag{A.4}$$

and the second order partial derivative is,

$$4\pi G^c_{ij,kl'}(\mathbf{x},\mathbf{x}') = (-\delta_{ij}\phi_{,kl} + \frac{\psi_{,ijkl}}{4(1-\nu^p)}) - A^c\delta_{ij}\phi_{,kl} - WB^c(\delta_{i3}\delta_{jm} - \delta_{j3}\delta_{im})\alpha^c_{,mkl} \\ + D^c\psi_{,ijkl} + \chi x_3 F^c\alpha^c_{,ijkl} + \chi\delta_{k3}F^c\alpha^c_{,ijl} + (G^c + B^c)Q_I\beta^c_{,ijkl} \tag{A.5}$$

where $\chi = 1$ when $x_3' > 0$ and $\chi = -1$ when $x_3' < 0$.

Appendix B. Comparison of numerical results in Section 5.2

This appendix aims to provide numerical comparisons among solutions with different Gauss integral points and support the correctness and stability. Due to page limits, we only provide comparisons related to Section 5.2 on the solar panels. Shown in Fig B.20, solutions with three different numbers of Gauss integral points agree well with each other, despite minor discrepancy existing at the end point ($x_1 = 0.099$ m) of σ_{11} for the curve "Gauss - 4 - subdivision". In order to compare the contour plots between solutions with 8 Gauss integral points and 6 Gauss integral points with subdivision scheme, the number of ticks of the color bar is set equal. It is observed very minor difference between Fig. B.21(c) and Fig. 12(c) that the maximum values are 11.97 and 11.98, respectively.

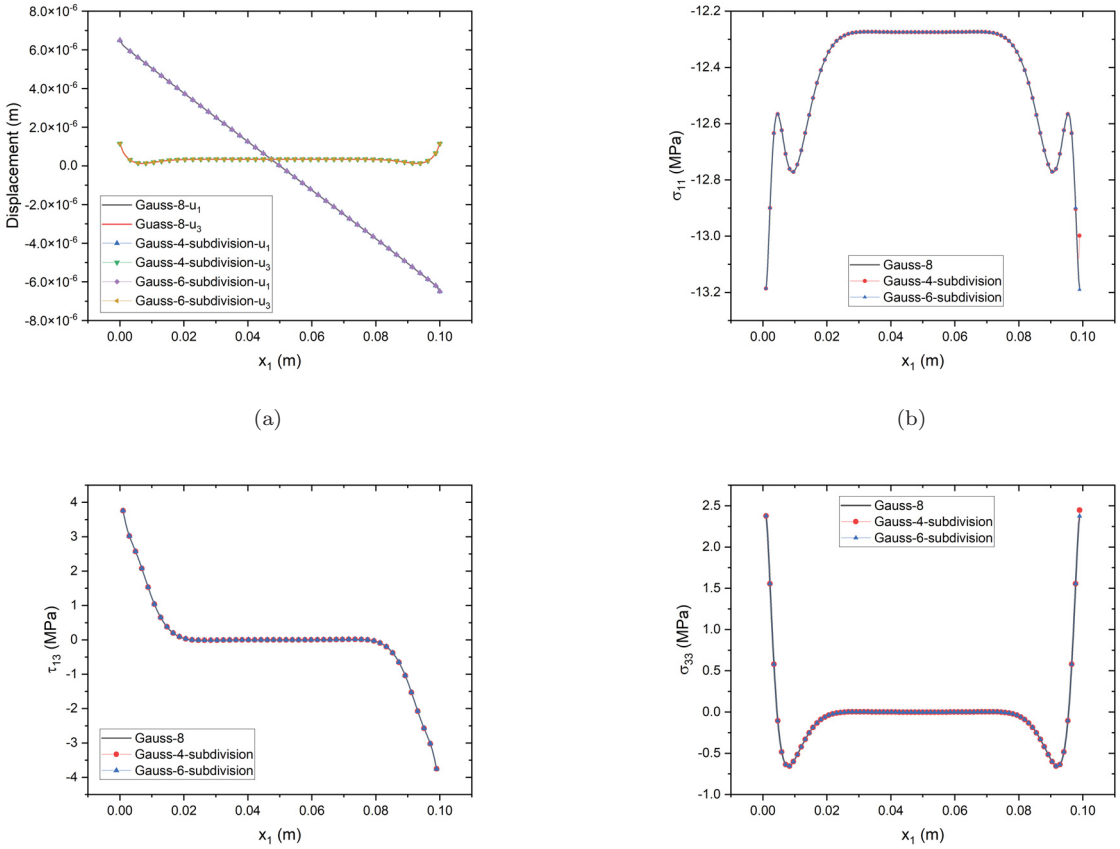

(a) (b)

(c) (d)

Figure B.20: Comparison of numerical results (a) u_1 and u_3, (b) σ_{11}, (c) τ_{13} and (d) σ_{33} along the horizontal center line $x_1 \in [0.001, 0.099]$ m among solutions of 8 Gauss integral points and $4, 6$ Gauss integral points with subdivision scheme

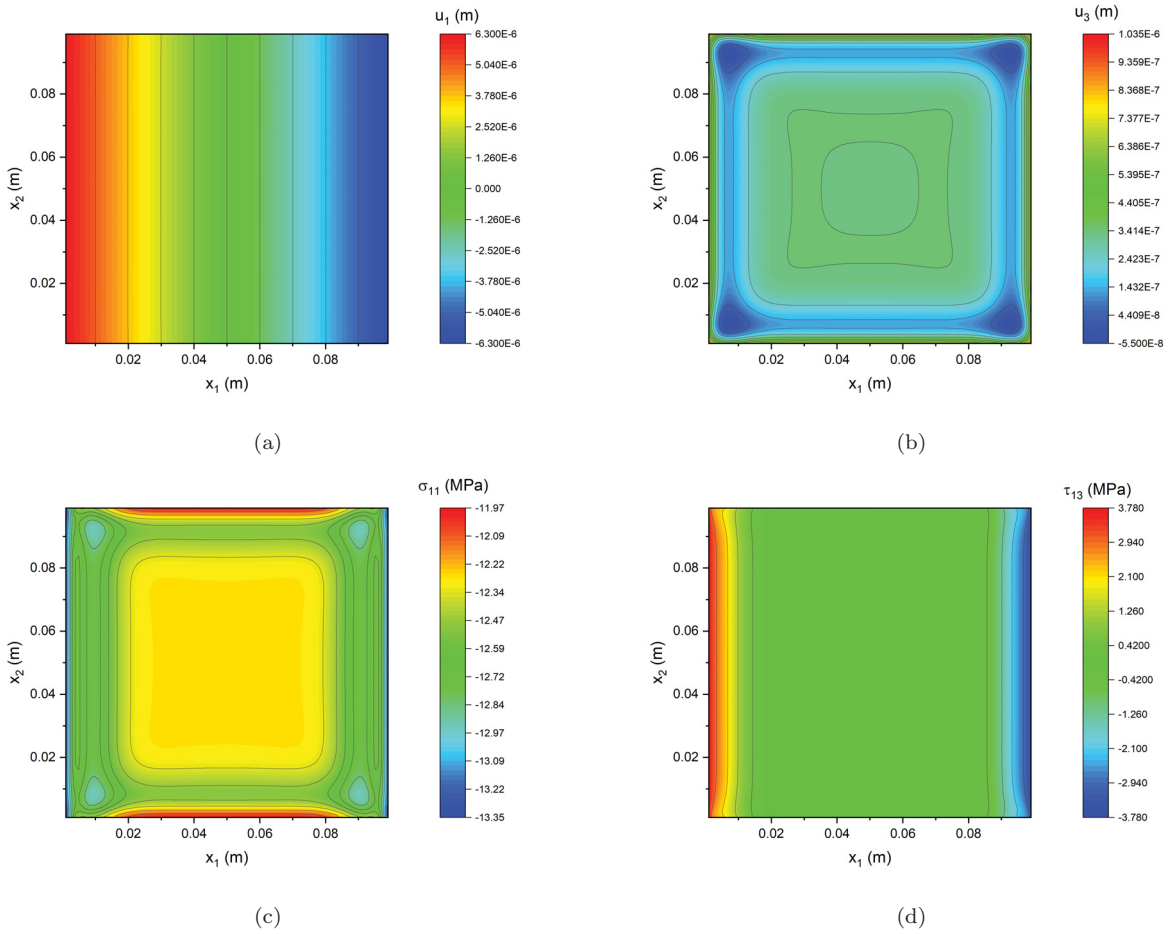

Figure B.21: Contour plots of solar panel (a) u_1, (b)u_3, (c) σ_{11} and (d) τ_{13} under thermal load within range $x_1 \in [0.001, 0.099]m$ and $x_2 \in [0.001, 0.099]m$ with solutions of 6 Gauss integral points with subdivision scheme

References

[1] J. H. Michell. The transmission of strees across a plane of discontinuity in an isotropic elastic solid, and the potential solutions for a plane boundary. *Proceedings of the London Mathematical Society*, s1-31(1):183–192, apr 1899.

[2] A. E. H. Love. *A Treatise on the Mathematical Theory of Elasticity.* Cambridge University Press, January 2013.

[3] A K Head. Edge dislocations in inhomogeneous media. *Proceedings of the Physical Society. Section B*, 66(9):793–801, sep 1953.

[4] Raymond D. Mindlin. Force at a point in the interior of a semi-infinite solid. *Physics*, 7(5):195–202, may 1936.

[5] Raymond D. Mindlin and David H. Cheng. Nuclei of strain in the semi-infinite solid. *Journal of Applied Physics*, 21(9):926–930, sep 1950.

[6] Leif Rongved. Force at point in the interior of a semi-infinite solid with fixed boundary. *Journal of Applied Mechanics*, 22(4):545–546, dec 1955.

[7] Leif Rongved. Force interior to one of two jointed semi-infinite solids. In *Proc. 2nd Midwestern Conf. on Solid Mechanics,Lafayette, IN*, 1955.

[8] H. H. Kuo and T. Mura. Circular disclinations and interface effects. *Journal of Applied Physics*, 43(10):3936–3942, oct 1972.

[9] J. Dundurs and N. J. Salamon. Circular prismatic dislocation loop in a two-phase material. *Physica Status Solidi (b)*, 50(1):125–133, mar 1972.

[10] N. J. Salamon and J. Dundurs. Elastic fields of a dislocation loop in a two-phase material. *Journal of Elasticity*, 1(2):153–164, dec 1971.

[11] Raymond D. Mindlin and David H. Cheng. Thermoelastic stress in the semi-infinite solid. *Journal of Applied Physics*, 21(9):931–933, sep 1950.

[12] BIBHUTIBHUSAN SEN. Note on the stresses produced by nuclei of thermo-elastic strain in a semi-infinite elastic solid. *Quarterly of Applied Mathematics*, 8(4):365–369, jan 1951.

[13] H.Y.YU and S.C.Sanday. Elastic fields in joined half-spaces due to nuclei of strain. *Proceedings of the Royal Society of London. Series A: Mathematical and Physical Sciences*, 434(1892):503–519, sep 1991.

[14] H. Y. Yu, S. C. Sanday, and B. B. Rath. Thermoelastic stresses in bimaterials. *Philosophical Magazine A*, 65(5):1049–1064, may 1992.

[15] Stefano Tinti and Alberto Armigliato. Single-force point-source static fields: an exact solution for two elastic half-spaces. *Geophysical Journal International*, 135(2):607–626, nov 1998.

[16] S. J. Singh, G. Kumari, and K. Singh. Displacements and stresses due to a single force in a half-space in welded contact with another half-space. *Geophysical Journal International*, 139(2):591–596, nov 1999.

[17] W. D. Collins. Some elastic and thermoelastic stress distributions in a semi-infinite solid. *Mathematika*, 7(2):149–160, dec 1960.

[18] L.J. Walpole. An elastic singularity in joined half-spaces. *International Journal of Engineering Science*, 34(6):629–638, may 1996.

[19] Tengxiang Wang, Chunlin Wu, Liangliang Zhang, and Huiming Yin. The green's function based thermal analysis of a spherical geothermal tank in a semi-infinite domain (under review). *Journal of Applied Mechanics*, Apr 2022.

[20] Huiming Yin, Gan Song, Liangliang Zhang, and Chunlin Wu. *The Inclusion-Based Boundary Element Method (iBEM)*. Elsevier, May 2022.

[21] Kefu Huang and Minzhong Wang. Elastic fundamental solutions to two jointed half-spaces. *Science in China Series A-Mathematics, Physics, Astronomy & Technological Science (in Chinese)*, 21(1):41–46, jan 1991.

[22] Sha Xiao, Zhongqi Quentin Yue, and Hongtian Xiao. Boundary element analysis of transversely isotropic bi-material halfspaces with inclined planes of isotropy and interfaces. *International Journal for Numerical and Analytical Methods in Geomechanics*, 43(17):2599–2627, aug 2019.

[23] Y.-C. Pan and T.-W. Chou. Point force solution for an infinite transversely isotropic solid. *Journal of Applied Mechanics*, 43(4):608–612, dec 1976.

[24] Mark T. Hanson. Elastic fields for point and partial line loading in transversely isotropic linear elasticity. *Journal of Elasticity*, 55(2):143–162, 1999.

[25] Jyh-Jong Liao, Tin-Bin Hu, and Cheng-Der Wang. Elastic solutions for an inclined transversely isotropic material due to three-dimensional point loads. *Journal of Mechanics of Materials and Structures*, 3(8):1521–1547, oct 2008.

[26] Ling Zhang, Haojiang Ding, and Weiqiu Chen. *Elasticity of Transversely Isotropic Materials*. Springer-Verlag New York Inc., March 2006.

[27] Y.-C. Pan and T.-W. Chou. Green's functions for two-phase transversely isotropic materials. *Journal of Applied Mechanics*, 46(3):551–556, sep 1979.

[28] Z.Q. Yue. Elastic fields in two joined transversely isotropic solids due to concentrated forces. *International Journal of Engineering Science*, 33(3):351–369, feb 1995.

[29] C. D. Wang and J. J. Liao. Elastic solutions for a transversely isotropic half-space subjected to buried asymmetric-loads. *International Journal for Analytical Methods in Geomechanics*, 1999.

[30] Cheng-Der Wang and Jyh-Jong Liao. Elastic solutions for stresses in a transversely isotropic half-space subjected to three-dimensional buried parabolic rectangular loads. *International Journal for Numerical and Analytical Methods in Geomechanics*, 26(14):1449–1476, 2002.

[31] Mark T. Hanson and Yang Wang. Concentrated ring loadings in a full space or half space: solutions for transverse isotropy and isotropy. *International Journal of Solids and Structures*, 34(11):1379–1418, apr 1997.

[32] H. T. Xiao and Z. Q. Yue. Elastic fields in two joined transversely isotropic media of infinite extent as a result of rectangular loading. *International Journal for Numerical and Analytical Methods in Geomechanics*, 37(3):247–277, nov 2011.

[33] K.M. Liew, J. Liang, H.J. Ding, and C. Lu. Elastic fields in two-joined half-spaces subject to point force and uniform ring loads. *Computer Methods in Applied Mechanics and Engineering*, 190(29-30):3749–3769, apr 2001.

[34] Zhong Qi Yue. On generalized kelvin solutions in a multilayered elastic medium. *Journal of Elasticity*, 40(1):1–43, jul 1995.

[35] Zhong qi Quentin Yue. Yue's solution of classical elasticity in n-layered solids: Part 1, mathematical formulation. *Frontiers of Structural and Civil Engineering*, 9(3):215–249, sep 2015.

[36] Zhong qi Quentin Yue. Yue's solution of classical elasticity in n-layered solids: Part 2, mathematical verification. *Frontiers of Structural and Civil Engineering*, 9(3):250–285, sep 2015.

[37] Muhammad Treifi and S. Olutunde Oyadiji. Evaluation of mode III stress intensity factors for bi-material notched bodies using the fractal-like finite element method. *Computers & Structures*, 129:99–110, dec 2013.

[38] Muhammad Treifi and S. Olutunde Oyadiji. Bi-material v-notch stress intensity factors by the fractal-like finite element method. *Engineering Fracture Mechanics*, 105:221–237, jun 2013.

[39] Himanshu Pathak, Akhilendra Singh, and Indra Vir Singh. Numerical simulation of bi-material

interfacial cracks using EFGM and XFEM. *International Journal of Mechanics and Materials in Design*, 8(1):9–36, oct 2011.

[40] L. Bouhala, Q. Shao, Y. Koutsawa, A. Younes, P. Núñez, A. Makradi, and S. Belouettar. An XFEM crack-tip enrichment for a crack terminating at a bi-material interface. *Engineering Fracture Mechanics*, 102:51–64, apr 2013.

[41] K. Kaddouri, M. Belhouari, B. Bachir Bouiadjra, and B. Serier. Finite element analysis of crack perpendicular to bi-material interface: Case of couple ceramic–metal. *Computational Materials Science*, 35(1):53–60, jan 2006.

[42] Y. J. Liu, S. Mukherjee, N. Nishimura, M. Schanz, W. Ye, A. Sutradhar, E. Pan, N. A. Dumont, A. Frangi, and A. Saez. Recent advances and emerging applications of the boundary element method. *Applied Mechanics Reviews*, 64(3), may 2011.

[43] Gernot Beer, Ian Smith, and Christian Duenser. *The Boundary Element Method with Programming*. Springer Vienna, 2008.

[44] Changzheng Cheng, Zhongrong Niu, and Naman Recho. Analysis of the stress singularity for a bi-material v-notch by the boundary element method. *Applied Mathematical Modelling*, 37(22):9398–9408, nov 2013.

[45] Zhang Yaoming Gu Yan. Boundary element analysis of complex stress intensity factors of bimaterial interface cracks. *Chinese Journal of Theoretical and Applied Mechanics*, 2021.

[46] O.J.B. Almeida Pereira and P. Parreira. Direct evaluation of cauchy-principal-value integrals in boundary elements for infinite and semi-infinite three-dimensional domains. *Engineering Analysis with Boundary Elements*, 13(4):313–320, jan 1994.

[47] C.A.Brebbia and S.Walker. *Boundary Element Techniques in Engineering*. Elsevier, 1980.

[48] Zhi Yong Ai, Dong Liang Feng, and Yi Chong Cheng. BEM analysis of laterally loaded piles in multi-layered transversely isotropic soils. *Engineering Analysis with Boundary Elements*, 37(7-8):1095–1106, jul 2013.

[49] Zhi Yong Ai, Yuan Feng Chen, and Xiao Bin Jiang. Static analysis of vertically loaded pile group in multilayered transversely isotropic soils. *International Journal for Numerical and Analytical Methods in Geomechanics*, 44(15):2114–2131, jul 2020.

[50] Sha Xiao and Zhongqi Quentin Yue. Boundary element formulation of axisymmetric problems in vertically non-homogeneous solids subject to normal traction. *Engineering Analysis with Boundary Elements*, 114:178–195, may 2020.

[51] R. Yuuki, S.B. Cho, T. Matsumoto, and H. Kisu. Efficient boundary element elastostatic analysis using hentenyi's fundamental solution. *Transaction of the JSME Series A*, 53(492):1581–1589, 1987.

[52] Z.W. Lou and M. Zhang. Elastoplastic boundary element analysis with hentenyi's fundamental solution. *Engineering Analysis with Boundary Elements*, 10(3):231–239, 1992.

[53] T Mura. Micromechanics of defects in solids (martinus nijhoff, dordrecht, 1987). *and*, 179:149, 1987.

[54] Y. J. Liu, G. Song, and H. M. Yin. Boundary effect on the elastic field of a semi-infinite solid containing inhomogeneities. *Proceedings of the Royal Society A: Mathematical, Physical and Engineering Sciences*, 471(2179):20150174, jul 2015.

[55] E. Pan and F.G. Yuan. Three-dimensional green's functions in anisotropic bimaterials. *International Journal of Solids and Structures*, 37(38):5329–5351, sep 2000.

[56] Changduk Kong, J Bang, and Y Sugiyama. Structural investigation of composite wind turbine blade considering various load cases and fatigue life. *Energy*, 30(11-12):2101–2114, 2005.

[57] Xiao-Wei Gao. Boundary element analysis in thermoelasticity with and without internal cells. *International Journal for Numerical Methods in Engineering*, 57(7):975–990, 2003.

[58] N. N. V. Prasad, M. H. Aliabadi, and D. P. Rooke. The dual boundary element method for thermoelastic crack problems. *International Journal of Fracture*, 66(3):255–272, apr 1994.

[59] Huiming Yin, Mehdi Zadshir, and Frank Pao. *Building Integrated Photovoltaic Thermal Systems*. Elsevier, 2021.

[60] H. M. Yin, G. H. Paulino, and W. G. Buttlar. An explicit elastic solution for a brittle film with periodic cracks. *International Journal of Fracture*, 153(1):39–52, sep 2008.